21

Quantitative analysis of alloy structures solidified under limited diffusion conditions

Hani Henein, Arash Ilbagi, Charles-André Gandin

21.1 The need for an instrumented drop tube

More than 90% of all metallic materials are manufactured starting from their liquid state. Designing the solid structure produced during solidification can have major savings in downstream processing. This is evident in the continued development of near-net shape processing. Examples such as shape castings, strip casting, powder processing and numerous welding and joining processes form part of that development. These processing routes offer great advantages to reduce cost of processing due to the refined structure of the solidified alloy, formation of metastable structures or reduced macrosegregation. In these processes, melt undercooling can play a major role in determining the final solidified structure or the type and morphology of precipitates. Under undercooled liquid conditions, there are numerous feasible paths which are also affected by interdependent and complex transport issues of alloy chemistry, heat, momentum and mass transfer. Each path may achieve a different solidified structure. Empirical approaches to optimize near-net shaping routes in materials processing from the liquid state are expensive and time consuming. The development of experimentally verified models of solidification under a wide range of conditions would provide a large leap forward in developing cost effective manufacturing strategies with products having superior properties. Such models must provide reliable information verified by experiments to describe any solidification pathway from the melt.

In order to develop such models, a reliable, robust and reproducible experimental technique is required. Such a capability must meet the requirements of a range of experimental conditions such as temperature, melt reactivity and composition, gas atmosphere, total pressure of gas, predictable and reproducible transport conditions for the solidifying sample and controlled and reproducible size of the sample. Electromagnetic levitation (EML) of droplets can meet many of these requirements. EML allows for direct observation of undercooling and solidification and can achieve very high undercoolings of large droplets (~6mm) that solidify in a containerless environment. However, EML alone cannot provide many of the desired quantitative data required for validating mathematical models of the evolution of microstructure during rapid solidification. For example, most of the volume of the droplet experiences a relatively low cooling rate. Also, the solidification of a droplet in such a system is strongly disturbed by large stirring effects from the electromagnetic forces used for positioning and heating the sample. Working with smaller sized droplets would be ideal.

A combination of rapid cooling, containerless solidification and low gravity can be achieved during the falling of micron sized molten droplets in a drop tube. This technique has been used quite extensively to study containerless solidification of materials [1, 2]. The drop tube provides the simplest, safest and least expensive way of obtaining microgravity environment. The level of microgravity achievable using this technique is relatively high, i.e. up to 1×10^{-5} of the earth's gravity [3], which is difficult to reach in other microgravity platforms, and the test is reproducible. However, the duration of microgravity supplied by drop tubes is short and many of the samples tested cannot solidify while falling in an evacuated drop tube. For example, the temperature of a 2 mm droplet of aluminum with overheating of 0.1 T_m (melting point) decreases only 19 K during 50 meters falling height [4]. Therefore, usually gases are introduced into the tube to ensure solidification of the falling molten droplets at the expense of deteriorating the low gravity level. In this condition, the smaller the sample size, the higher the gas pressure and the faster the initial falling velocity, the quicker the microgravity condition disappears. However, in spite of losing the microgravity condition as a result of the

Containerless Unidercooling of Drople and Droples. Edited by D.M. Herlach and D. M. Matson
Copyright © 2011 WILEY-VCH Verlag GmbH & Co. KGaA, Weinheim
ISBN 978-3-527-33122-2

drag force applied on the particles, the solidification of materials in a drop tube filled with cooling gas is of great interest due to the containerless and high cooling rate conditions it supplies. Also, since the heat transfer conditions for movement of a hot spherical body in stagnant fluid is well understood, it is feasible to use experimental data to validate droplet cooling models. For this purpose, in larger drop tube facilities, photodetectors are arranged at various places along the drop tube to measure the cooling rate and the sudden increase of temperature during recalescence. The latter is of great importance as it allows for evaluating the undercooling prior to nucleation. In drop tubes of smaller sizes, however, due to practical difficulties, it has been a common belief that it is not possible to record the thermal history during the solidification of the individual droplets. Apart from the thermal history, in-situ measurement of the droplets diameter, initial velocity and instantaneous velocity is crucial in validating the heat transfer models.

Melt atomization is another approach to consider. Melt atomization is a technique used for containerless processing of melts, in which the melt is disintegrated by high pressure gas or by electrohydrodynamic fields. Melt atomization can create droplets with diameters of only few microns. High degrees of cooling rate and undercooling can be achieved using this technique. However, it is shown that there is significant velocity gradient in both radial and axial directions [5, 6], which vary according to the design of the atomization unit (e.g. the design of gas nozzles and the relative positioning between gas jets in gas atomization). Thus, a wide droplet size distribution is achieved and each droplet finds itself in a different local gas velocity and temperature. Consequently, depending on how the droplets couple and move with the atomizing gas, the evolution of chemistry and/or microstructure varies. This makes it very difficult to identify how individual process variables can affect the resulting characteristics of individual, or group of, droplets [7]. A containerless solidification system based on a single fluid atomization approach can satisfy these requirements.

In recent years, atomization of melts (high temperature fluids such as metals, alloys and slags) has seen significant innovative revolutionary new breakthroughs, developments and capabilities. These are primarily with the single fluid atomization approach where a melt stream is rendered unstable by Rayleigh instability in a static gas atmosphere or where individual drops are generated. Under the right atomizing conditions, a mono-size or a controlled and narrow size distribution of droplets is generated [8-12]. The droplets are either allowed to fall through a stagnant gas atmosphere and solidify or are deposited onto a substrate. This may be achieved by allowing the droplets to free fall through a stagnant gas, in a vacuum or reduced pressure in the vessel.

The method that will be the focus of this Chapter is Impulse Atomization (IA) [13]. Using conventional refractory materials, impulses are mechanically applied to a melt with low frequency and high amplitude (Figure 21-1). These impulses feed the melt through the orifices and provide the melt stream with the required instability for breakup. Thus, discrete lengths of streams generated from an orifice, breakup into droplets. Since the droplets accelerate under gravity, no droplet collisions occur despite a narrow spray angle (~5^o). Atomization has been carried out on a wide range of alloys of Pb, Sn, Zn, Al, Cu, Ni, Co and various steels. Powders and granules have been produced with median size (d_{50}) of 100μm to 1.5mm and a lognormal distribution, (d_{84}/d_{50}), of about 1.4 using up to100 orifices in nozzle plates of 2.5 cm diameter [14-16].

A more detailed description of IA and the instrumentation available for diagnostics will be presented in this chapter, this will be followed by a summary of the experimental results and characteristics of the samples generated using IA. A detailed analysis of the transport conditions in IA will be outlined; then some results of quantitative analysis of microstructure evolution of various binary systems will be presented for both eutectic and peritectic systems. The industrial relevance of these results will be discussed at the end of this Chapter.

21.2 Description of IA

IA was developed and patented [13, 17] at the University of Alberta, Canada. It is a single-fluid atomization technique where a melt stream is generated by pushing the melt out of orifice(s) using a refractory plunger. Repeated application of this pressure at low frequency and high amplitude generates droplets as small as 100

Contairnerless Unidercooling of Drople and Droples. Edited by D.M. Herlach and D. M. Matson
Copyright © 2011 WILEY-VCH Verlag GmbH & Co. KGaA, Weinheim
ISBN 978-3-527-33122-2

µm [16]. The generated droplets spheroidize and lose heat to the surrounding stagnant gas of choice while falling through a 4-meter-long drop tube. Schematics of the process and of the apparatus are shown in Figure 21-1. In this figure, the impulse generator, the plunger (driver), a metal tundish system and a nozzle plate complete with orifices are shown as well as a schematic of the instrumented drop tube.

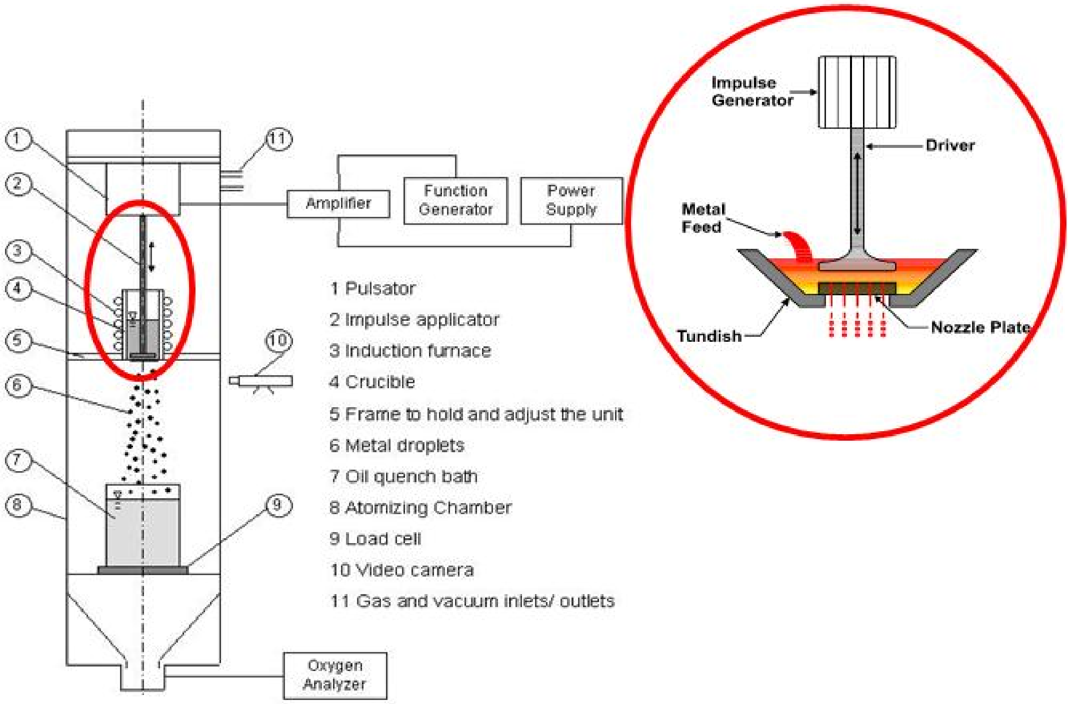

Figure 21-1: Schematic of IA unit.

IA is used to produce rapidly solidified metallic (or non-metallic) droplets and powders. This process can reproducibly yield powders of uniform size-distribution with cooling rate as high as 10^4 K/s [13, 18]. The process has successfully been employed to produce a wide range of metal droplets including zinc, magnesium, neodymium-iron, lead-tin alloys, aluminum alloys, copper alloys, low carbon steel and tool steel.

Previously the most attractive benefits of on-line sizing and its application in gas atomization process control had been investigated [12-13]. It was shown that the implementation of the on-line measurement tools can lead to decreased operating costs and to higher yields of powder in a target size range. Such measurements in an IA system, where the droplet-gas heat transfer may be accurately characterized, can lead to valuable experimental data, which in turn can be used to validate the droplet solidification models.

A video camera, a two-color pyrometer custom-made for sprays and a shadowgraph have been implemented, which allow for measurement of droplets diameter, velocity and temperature. Figure 21-2 shows the velocity profile of a 3.3×10^{-4} m Al-17wt% Cu droplet. The velocity measured at the camera position was 2.17 m/s. This figure exemplifies the importance of having probes for velocity, size and temperature of falling droplets at various positions of atomization tower. In this case, measurement of the velocity allows for confirming the velocity profile achieved from the model and as a result, finding the initial and terminal velocity of the droplets. From Figure 21-2 the droplet almost reached its terminal velocity at the bottom of the atomization tower [13].

Contairnerless Unidercooling of Drople and Droples. Edited by D.M. Herlach and D. M. Matson
Copyright © 2011 WILEY-VCH Verlag GmbH & Co. KGaA, Weinheim
ISBN 978-3-527-33122-2

Measurement of the velocity and temperature coupled with the modeling of the solidification of a falling droplet would allow for evaluation of the degree of gravity during the solidification of the droplet.

Several different probes and sensors have also been implemented to collect data from different parts of the atomization tube. Thermocouples read the temperature of the melt within the tundish and the gas within the tube. An oxygen sensor measures the amount of remained oxygen in the tower. Two other probes measure the amplitude, acceleration and applied force of the moving plunger and a load cell at the bottom of the drop tube measures the mass flow rate.

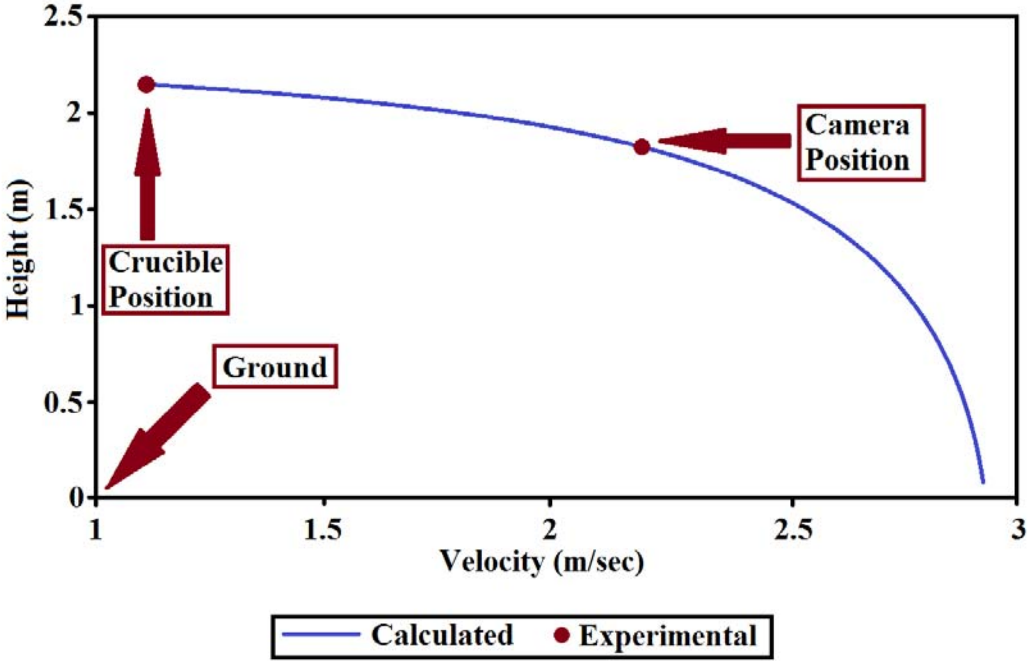

Figure 21-2. Velocity profile of a 3.3×10^{-4} m Al-17 wt%Cu droplet with an initial velocity of 1.13 m/sec [13].

21.3 Powder characteristics

The break up mechanism in IA has been reported by Henein [16] and Yuan [13]. In IA, discontinuous streams, called ligaments, are produced by an impulse applicator. Without the application of the impulses no molten metal comes out of the orifices. Ligaments are formed out of the orifices during the downward cycle of an impulse. During the other half cycle of an impulse no fluid emanates from the orifices. The discharged ligaments have a sinusoidal natural disturbance on their surface due to the exit velocity of the ligament from the orifice and the applied frequency. The disturbance will have a wavelength λ. According to Rayleigh instability, the minimum theoretical wavelength of the disturbance required for breakup of a liquid stream is $\lambda=\pi d$, where d is the diameter of the ligament, or in other word, the orifice. Hence, if the length of the ligament is smaller than its circumference, the ligament is expected to form only one droplet, and if it is larger than the circumference, the ligament will break up. It has been experimentally observed in IA that each ligament breaks up into several droplets [13].

It is possible to estimate the number of droplets that are formed from a discrete stream. From the mass flow rate measured by a load cell placed at the bottom of the IA drop tube, one can estimate the volumetric flow rate of the melt per orifice, and in turn the length of ligament and its exit velocity. The average exit velocity has been found to be around 0.5 m s^{-1}, which has been a confirmed using video imaging technique (e.g. Figure 21-2). This yields a mass flow flux for aluminum in the range between 2000 and 3000 kg m^{-2} s^{-1}. Dividing the exit velocity by the applied frequency will yield an estimate of the ligament length to be of the order of 4-5 mm.

Contairnerless Unidercooling of Drople and Droples. Edited by D.M. Herlach and D. M. Matson
Copyright © 2011 WILEY-VCH Verlag GmbH & Co. KGaA, Weinheim
ISBN 978-3-527-33122-2

Hence, each ligament will break up. If an inert atmosphere or vacuum is present in the chamber below the orifice, these ligaments will spherodize and begin their trajectory to the bottom of the chamber. The exit velocity is also important as it affects the level of achievable low gravity and it affects the rate of heat loss from the droplet.

By varying the impulse driver acceleration, the orifice size, orifice shape, melt temperature and gas atmosphere, the shape, size distribution and microstructure of the powders atomized can be manipulated to the required specifications. IA experiments have been carried out with as many as 97 orifices in a 2.5 cm nozzle plate, producing tailored mass median particle size (D_{50}) and controlled log-normal standard deviation (S.D.) (D_{84}/D_{50}) of $1.1 \leq \sigma \leq 1.6$ [16]. Figure 21-3 displays the mass mean (D_{50}) particle size as a function of orifice diameter for aluminum, copper and iron alloys produced using IA. From the slope of the solid line, which represents a linear regression analysis of the data, the ratio between particle size and orifice diameter is about 1.28. In addition, the log-normal S.D. of particle size (D_{84}/D_{50}) for the same alloys and orifices sizes is shown in Figure 21-4. For the alloys atomized, the S.D. lies primarily between 1.3 and 1.5. The results at about 1.9, 1.7 and 1.65 are considered outliers and occurred during early atomization trials with the iron, copper and aluminum alloys, respectively.

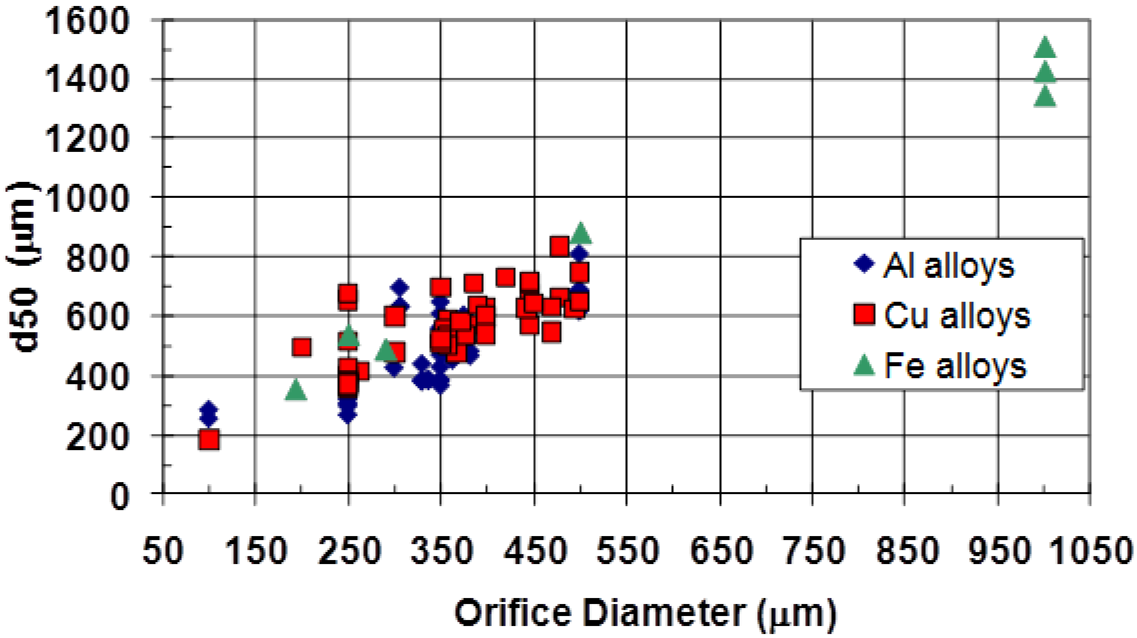

Figure 21-3. Mass mean (D_{50}) particle size as a function of atomizing orifice diameter [16].

Alloy composition also affects the mean droplet size. In Figure 21-5 the mass mean is plotted as a function of the iron content for binary aluminum alloys having iron content ranging from 0 wt% (commercially pure aluminum) to 1.9 wt% for samples atomized in nitrogen and helium. The trend is clear. The mass mean increases with the iron content. There is no appreciable effect of atomizing inert gas. It appears, therefore, that the presence of iron increases the surface tension of the alloy [19].

Figures 21-6 and 21-7 show the shape and surface structure of copper powders and an Al-17 wt% Cu powder atomized using IA. Both samples were atomized in a nitrogen atmosphere and show highly spherical shaped powders. The Al-17 wt%Cu sample clearly shows a very fine dendritic structure on the surface of the particle. Primary dendrite trunks, secondary dendrite arms are clearly visible. Quantifying the scale of the

Contairnerless Unidercooling of Drople and Droples. Edited by D.M. Herlach and D. M. Matson
Copyright © 2011 WILEY-VCH Verlag GmbH & Co. KGaA, Weinheim
ISBN 978-3-527-33122-2

microstructure and of the fraction of various phases present in these particles will provide valuable data for model verification.

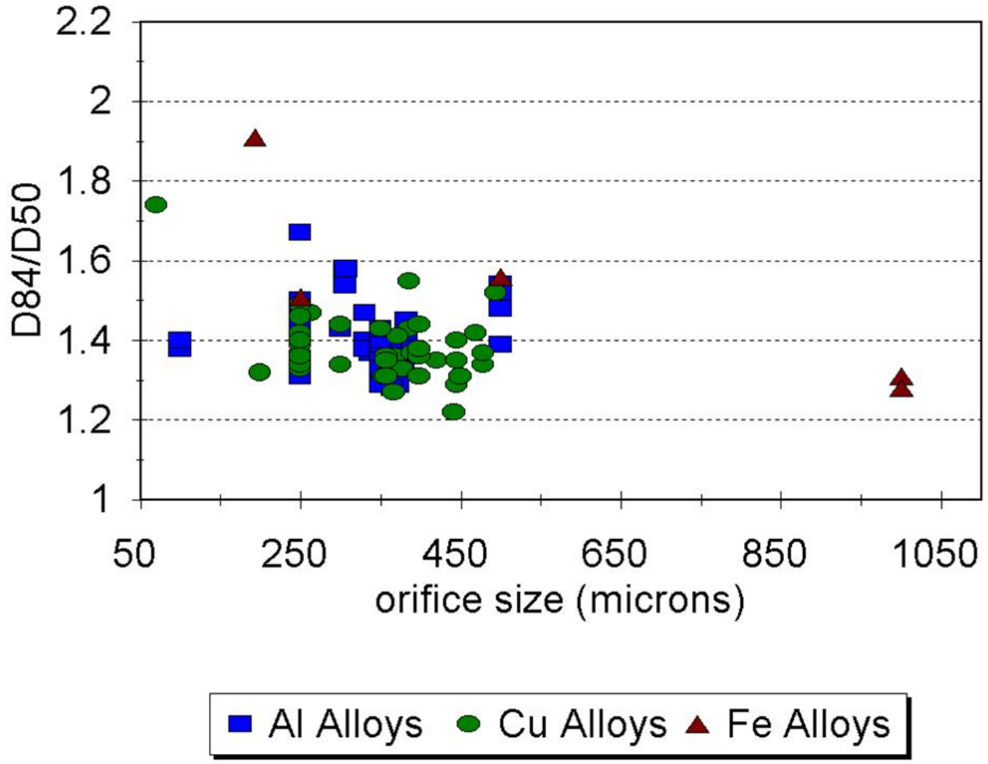

Figure 21-4. Log-normal standard deviation as a function of orifice size [16].

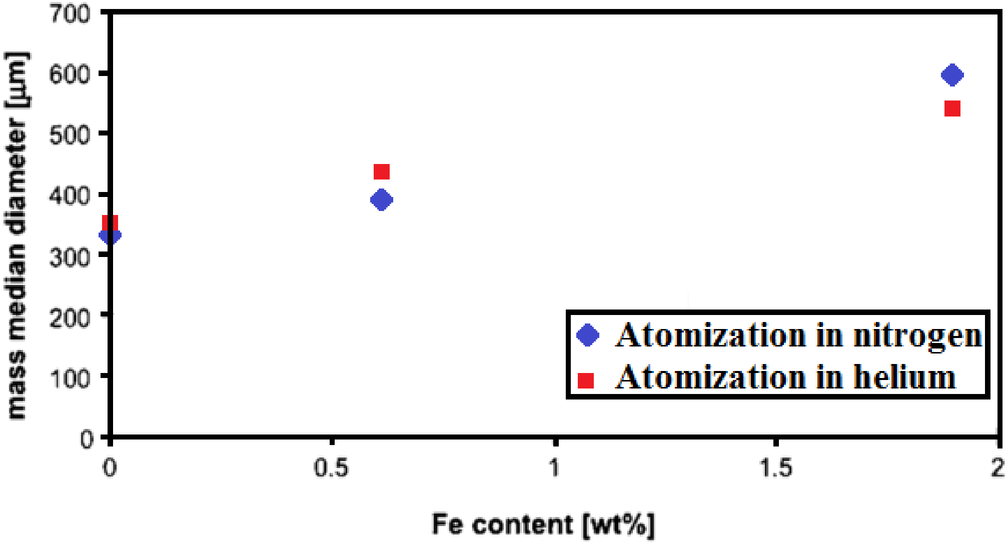

Figure 21-5. Mass median diameter as a function of the iron content in Al-Fe powders atomized in nitrogen and helium [19].

Contairnerless Unidercooling of Drople and Droples. Edited by D.M. Herlach and D. M. Matson
Copyright © 2011 WILEY-VCH Verlag GmbH & Co. KGaA, Weinheim
ISBN 978-3-527-33122-2

21.4 Quantification of Microstructure

In this section the numerous methods utilized to identify the various phases in the microstructure and to quantify their relative amounts will be presented. The methods used range from the very well established methods such as image analysis on images from scanning electron microscopy (SEM) to state of the art techniques. With SEM images, a sufficient number must be taken in order to ensure that the result is representative of the structure of the sample being studied. State of the art methods include 3 dimensional (3D) x-ray micro-tomography and neutron diffraction. For both special beam lines must be accessed in order to carry out the desired measurements. Subsequent to data collection of x-ray tomography from synchrotrons, rigorous image analysis must be carried out on large files (about 8 to 16 GB) representing the structure in micron sized particles. From these images, microstructural features such as dendrite trunks, nucleation sites or porosity may be isolated and quantified as to scale, relative amount and location for example. For neutron diffraction, Rietveld analysis is carried out to identify the phases present as well as their relative amounts. In this section all of these methods will be utilized to quantify the microstructure of a number of binary alloys studied.

21.4.1 Secondary dendrite arm spacing

Figure 21-8 shows a comparison of secondary dendrite arm spacing measurements done on different particle sizes obtained from different atomizing techniques. It is interesting to note that although Alcoa gas atomized powders and centrifugally atomized powders seemed to yield asimilar relationship between dendrite arm spacing and particle size, the powder generated using IA appears to have a finer structure than those from the other atomizing techniques. An etched cross section of an IA phosphorous bronze powder clearly shows two regions having structures with different length scales. The finer scale structure must have formed under faster cooling or dendrite growth conditions than the coarser structure. Quantifying the different phases and the scale of the structure is key to understanding the microstructure evolution under rapid solidification.

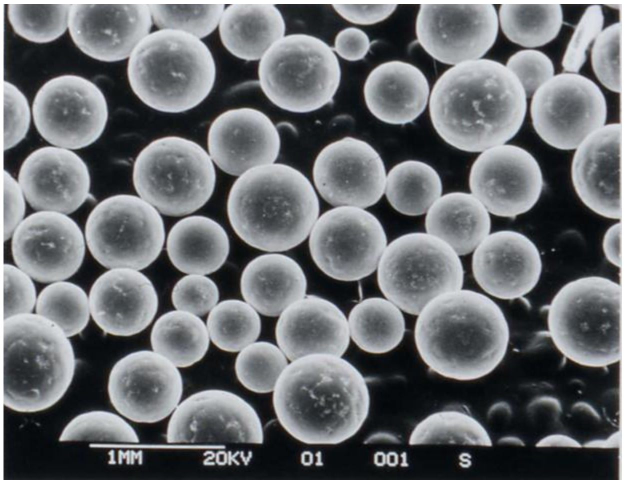

Figure 21-6 SEM image of IA copper powder that was atomized at 1200°C (run#060793) into a nitrogen atmosphere.

Contairnerless Unidercooling of Drople and Droples. Edited by D.M. Herlach and D. M. Matson
Copyright © 2011 WILEY-VCH Verlag GmbH & Co. KGaA, Weinheim
ISBN 978-3-527-33122-2

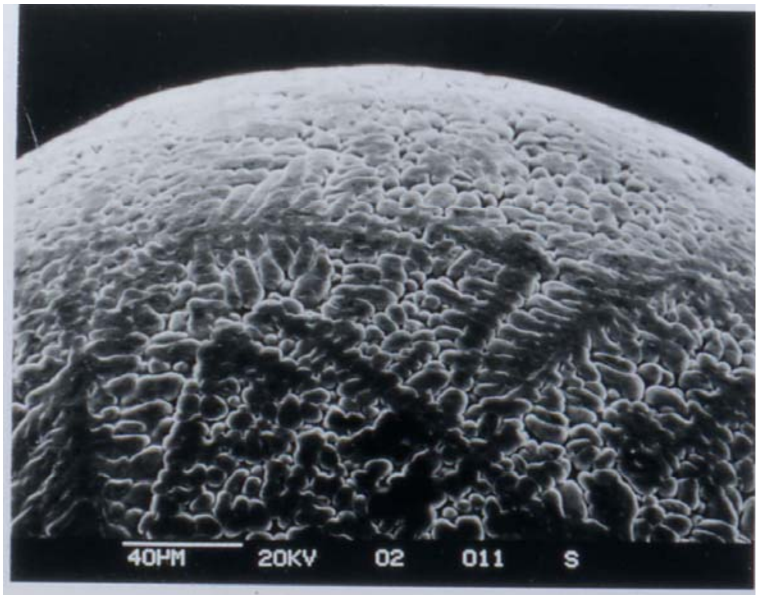

Figure 21-7: SEM image of a 475 μm IA-Al-17 wt% Cu powder that was atomized at 700°C (run#042893) into a nitrogen atmosphere.

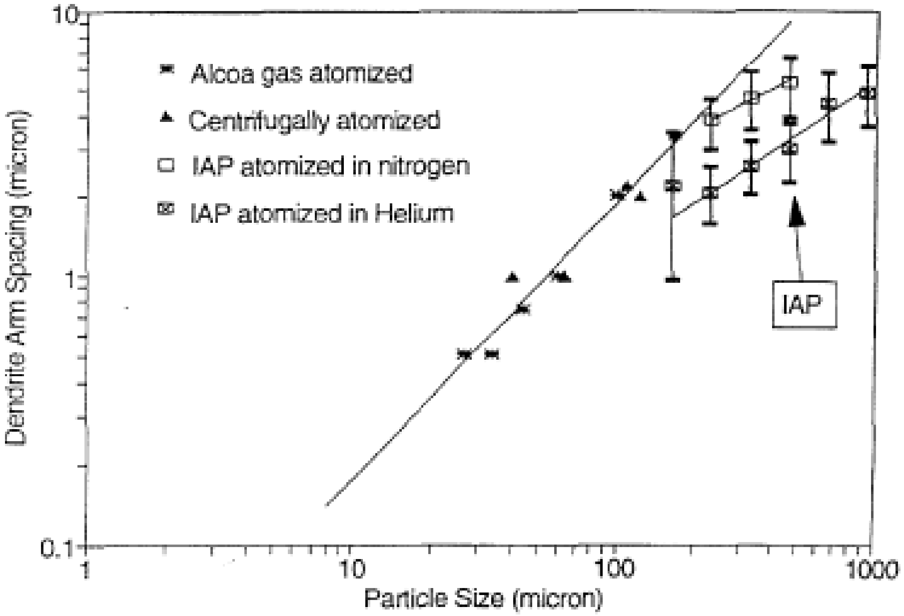

Figure 21-8: Comparison of the scale of the microstructure for difference atomization methods for an Al-Ni-Fe alloy.[20]

Contairnerless Unidercooling of Drople and Droples. Edited by D.M. Herlach and D. M. Matson
Copyright © 2011 WILEY-VCH Verlag GmbH & Co. KGaA, Weinheim
ISBN 978-3-527-33122-2

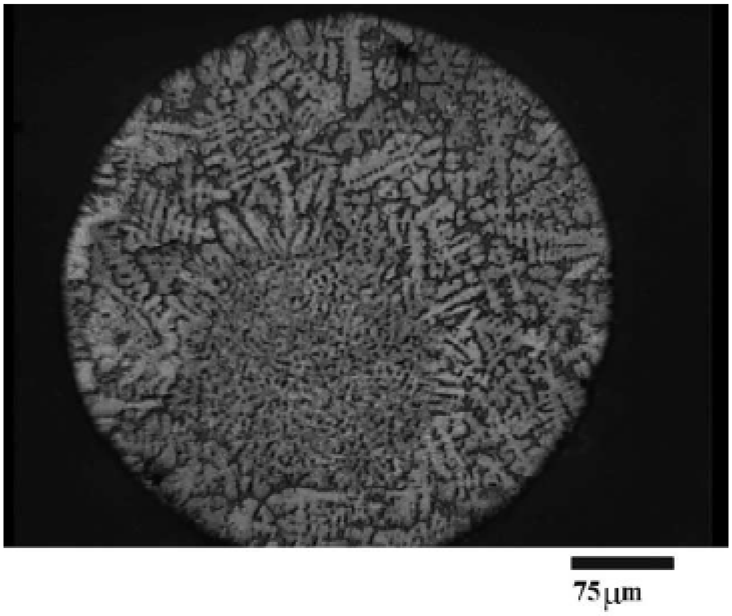

Figure 21-9: An etched cross section of an IA phosphorous bronze powder atomized in nitrogen at 950oC (971031). Two size scales of structure are evident [16].

Conlon et al. [21] studied the effect of the homogenous distribution of $CuAl_2$ phase in an Al matrix. They used IA to produce four different composition of Al-Cu alloys (5, 10, 17 and 24 wt%) in two different cooling gases, helium and nitrogen. Image processing techniques were utilized to measure the volume fraction of the eutectic structure. Their results are shown in Figure 21-10, where the equilibrium volume percent of $CuAl_2$ found from the Al-Cu phase diagram is shown with a solid line.

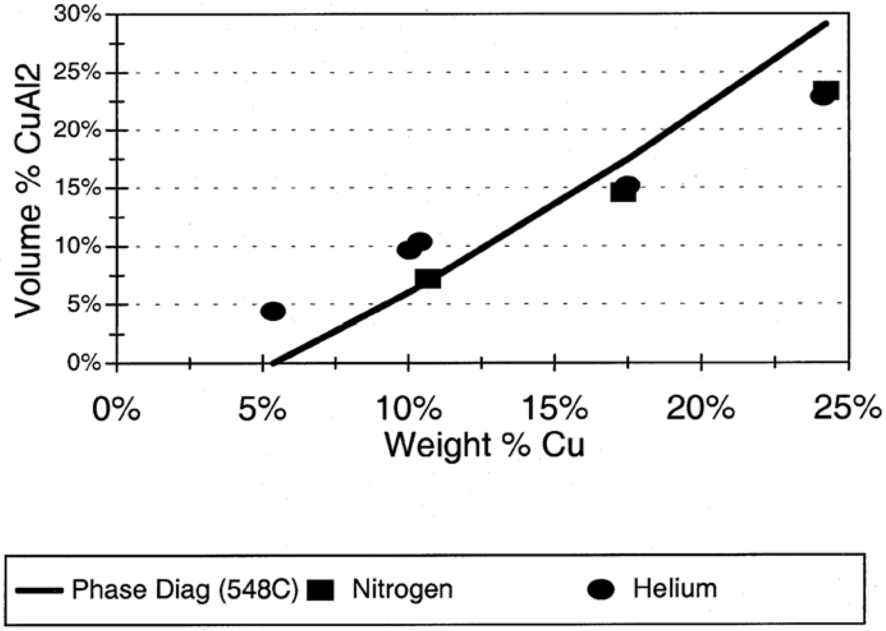

Figure 21-10. Volume fraction of $CuAl_2$ in helium and nitrogen atomized granules as a function of copper content [21].

Contairnerless Unidercooling of Drople and Droples. Edited by D.M. Herlach and D. M. Matson
Copyright © 2011 WILEY-VCH Verlag GmbH & Co. KGaA, Weinheim
ISBN 978-3-527-33122-2

It is evident that the experimental results of the 5 and 10 wt.% Cu are above the equilibrium line while those at 17 and 24 wt.% Cu are below. Previously Gill and Kurz had shown that both 5 and 10 wt% Cu alloys are in the single phase region. Thus, the higher $CuAl_2$ content indicates the microsegregation of Cu during solidification. At the higher Cu contents, however, the lower than equilibrium fraction of $CuAl_2$ is an indication of a metastable structure that would occur under rapid solidification conditions. Prasad et al. [21] then used micro-tomography techniques to identify regions of nucleation, recalescence and dendrite growth. These are discussed in more detail in this chapter.

In another study, von Freyberg et al. [7] compared the microstructure of Cu-6Sn powders produced using gas atomization with those from IA technique and found that for the same size of droplet fully solidified in gas, IA powders exhibit a finer microstructure than gas atomized powders. All these observation clearly indicate that IA technique generates rapidly solidified particles.

The rate of cooling has been shown to be dependent on the particle size, cooling gas and the composition of falling droplets. Henein et al [19] studied the droplet solidification of IA Al-0.61wt%Fe and Al-1.9wt%Fe. Figures 21-11 and 21-12 show the cell spacing measurements as a function of the average particle size for both compositions atomized in nitrogen and helium atmosphere. The plots clearly show that powders atomized in helium have finer cell spacing than those atomized in nitrogen. Also, cell spacing in the alloys with higher iron content is smaller than that of the alloy with lower iron content. In addition, the gap between the two increases with increasing the particle size.

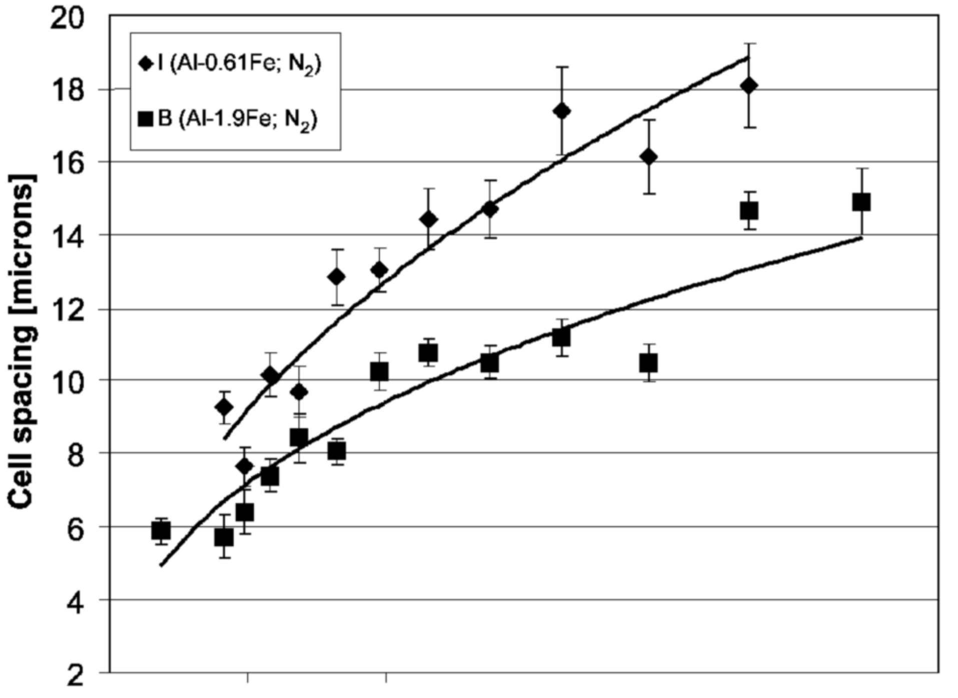

Figure 21-11: Effect of composition and particle size on the cell spacing for Al-0.61Fe and Al-1.9Fe alloys atomized in nitrogen [19].

Contairnerless Unidercooling of Drople and Droples. Edited by D.M. Herlach and D. M. Matson
Copyright © 2011 WILEY-VCH Verlag GmbH & Co. KGaA, Weinheim
ISBN 978-3-527-33122-2

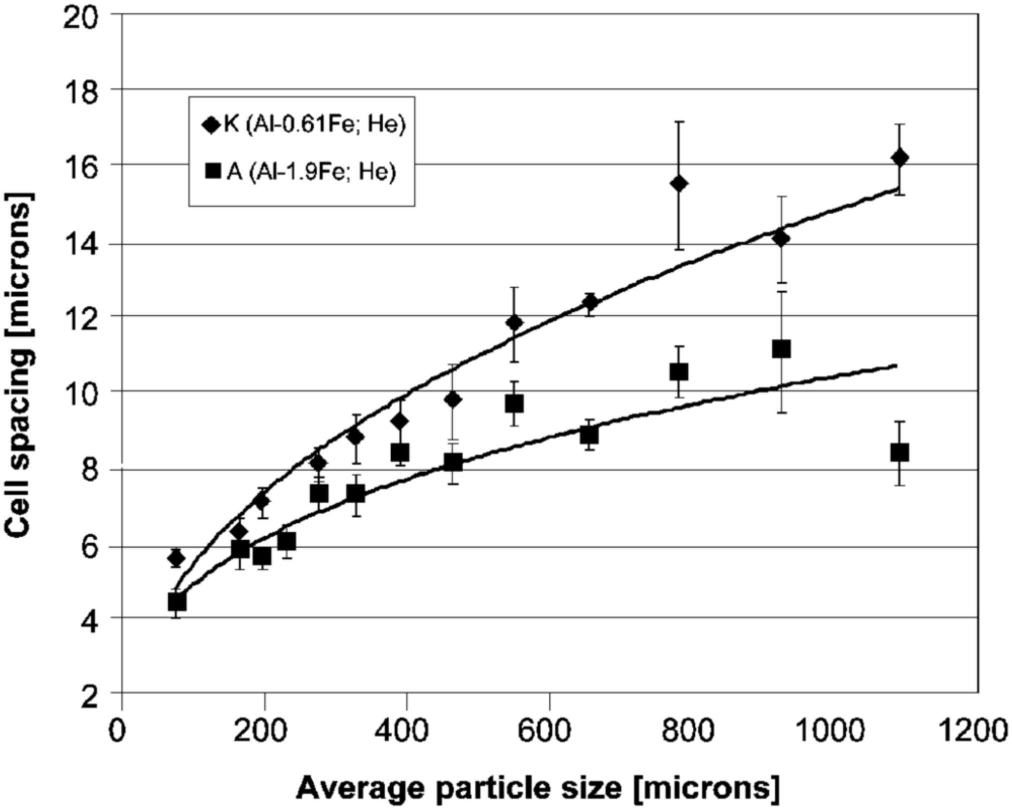

Figure 21-12: Effect of composition and particle size on the cell spacing for Al-0.61Fe and Al-1.9Fe alloys atomized in helium [19].

To better understand the solidification process of atomized droplets it is very important to utilize characterization techniques that can provide information about the whole volume of a droplet, or group of droplets. In the following two sections, applications of two important characterization techniques with such capabilities are discussed.

21.4.2. X-ray Micro-tomography

Microscopy can be used to gather information about solidification characteristics like cell spacing and micro segregation (using quantitative metallography), but is constrained by the small number of sections that can be viewed from a given sample.

Analysis of solidification characteristics like nucleation, recalescence, microsegregation and porosity formation in atomized droplets can be performed using a 3D visualization technique. It can provide information about the entire solidified volume. X-ray micro-tomography is a non-destructive technique that allows for gathering information from the entire sample volume. Hence, if a powder particle exhibits anisotropy in its structure such as shown in Figure 21-9, it will be clearly apparent using 3D X-ray micro-tomography. While using an SEM one would have to resort to a large number of samples of 2D cross-sections. Despite such efforts, a definitive determination of the microstrutural evolution of a droplet cannot be made.

The working principle of micro-tomography is based on X-ray radiography. The local fluctuations of the X-ray absorbance create the contrast that is observed in a simple X-ray projection. A number of radiographs taken under different viewing angles are combined to reconstruct a 3D map of the local attenuation coefficient of the

Contairnerless Unidercooling of Drople and Droples. Edited by D.M. Herlach and D. M. Matson
Copyright © 2011 WILEY-VCH Verlag GmbH & Co. KGaA, Weinheim
ISBN 978-3-527-33122-2

X-rays. A very high resolution stack of images, called slices, of the specimen is obtained by using an intense and highly energetic source.

Analysis and visualization of images obtained from X-ray micro-tomography requires a pre-processing procedure to separate individual particles from the background and other particles that may be sampled by the X-ray beam. Also X-ray beam creates artifacts that are necessary to be removed from the sample. It is because they have almost the same intensity in the final image as the porosity or some microstructural features. This introduces error into the quantitative analysis of the microstrucutre of a sample. Therefore, a clean mask file of the droplet must be generated and then applied to the original data to eliminate all but the structural features of interest. Application of this procedure preserves all the surface and microstructural details of the particle. [24]

Henein et al. [19] used this technique to study the eutectic in the droplets of Al-0.61Fe and Al-1.9Fe. A sequence of images of a 550 µm droplet of Al-0.61Fe from micro-tomography is shown in Figure 21-13. A single nucleation point for the entire droplet was identified very near the periphery of the surface of the droplet. The arrow in slice ‘1011’ points to the nucleation point. Also clearly visible are the primary dendrites growing from the region of nucleation and initial growth. The lighter color represents the eutectic in the droplet. It can be seen that in some regions in the droplet a higher eutectic fraction has formed. This is evident by the various shades of color in the sequence of images. From the images it was found that there are two regions where there is a high concentration of eutectic. These regions are obviously those that were last to solidify in the droplet. This was determined by imaging both these regions of high eutectic concentration and the regions of porosity. The 3D rendering of these images were superimposed as seen in Figure 21-14 and were observed to be coincident.

Prasad et al. also investigated the solidification of Al-Cu using the tomography technique [22, 23]. Observations were made on the droplet using X-ray beams of 1 µm resolution. X-Ray tomography was performed on the ID19 beam line at European Synchrotron Radiation Facility (ESRF) in Grenoble, France. Tomography was carried out on Al-5wt%Cu and Al-17wt%Cu atomized droplets of 500µm in diameter.

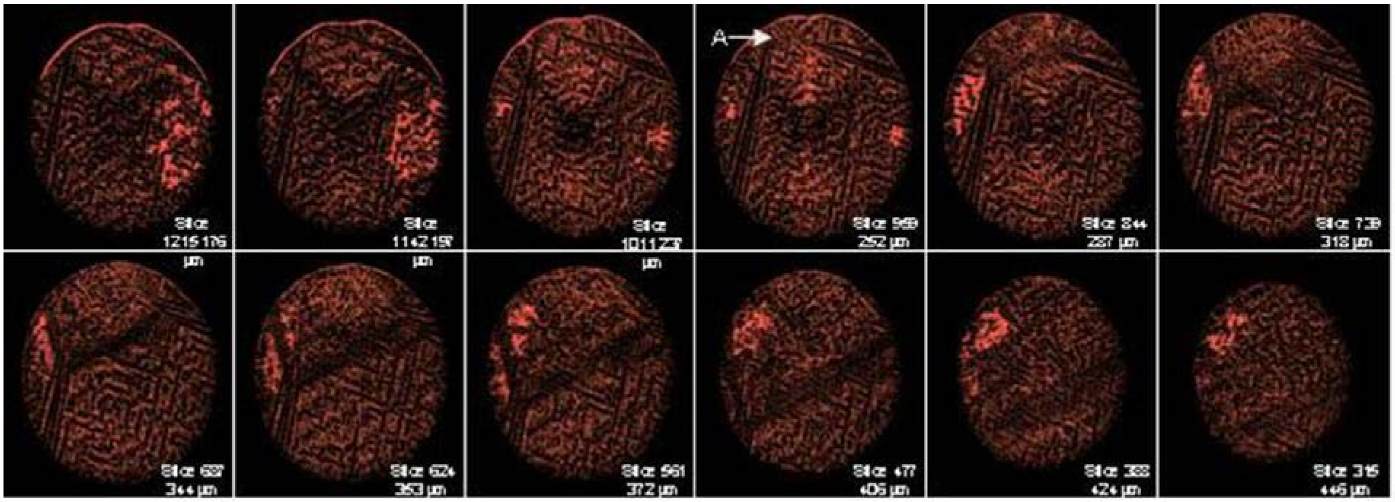

Figure 21-13: Tomographic images of Al-0.61Fe shown in a sequence of slices from of a 550 µm powder atomized in nitrogen. The lighter color in the particle represents the eutectic. Point A identifies the region where nucleation and initial growth was initiated [19].

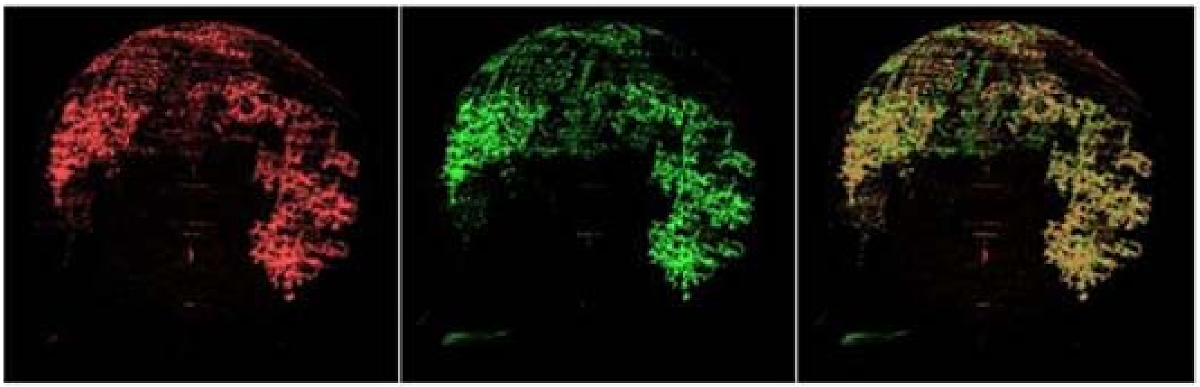

Figure 21-14: Full volumes of the 550 μm Al-0.61Fe particle highlighting the highest concentration of eutectic, porosity and a superimposition of eutectic and porosity.

The X-ray tomography provided additional information about solidification that was not possible to get from conventional 2D techniques. Using tomography images it was possible to clearly locate the nucleation site, which was found to be within the droplet, as it can be seen in Figure 21-15. Nucleation centers were approximately calculated for each of the droplets. The average distance between the droplet center and the nucleation site was 0.63 R_p for the Al-17wt%Cu droplet and 0.75 R_p for the Al-5wt%Cu droplet, where R_p is the radius of the individual droplet. This study also showed that none of the particles analyzed have multiple nucleation sites. This definitive conclusion illustrates one of the key advantages of the 3D micro-tomography technique over 2D visualization methods or serial sectioning techniques. Note that an additional advantage of 3D micro-tomography is that it is a non-destructive technique.

Recalescence boundaries characterized by fine dendrites were seen in all droplets and the volume fraction of recalescence in the droplets was evaluated. The fraction of droplet area covered by the fast growing fine dendrite structure was found to be larger for the Al-17wt%Cu than the Al-5wt%Cu droplets. The higher recalescence volume in Al-17wt%Cu droplet compared to that in Al-5wt%Cu droplet would correspond to higher growth velocities. Therefore, it is believed that the solidification has taken place at higher undercooling in Al-17wt%Cu droplet. The volume fraction of recalescence regions performed can be a useful guide for modeling purposes.

Furthermore, the Al-5wt%Cu droplet was found to have an overall coarser structure than the Al-17wt%Cu. This shows that the growth rate for Al-17wt%Cu alloy is higher than that of Al-5wt%Cu. The observation of difference in scale of microstructure within the whole body of the droplet is also useful for modeling since the total undercooling can be varied to get simulation results consistent with the experimental results. This will be further discussed in this chapter.

Micro-tomography can be used in analyzing solidification porosity. It can also be used to measure the volume fraction of the porosity within the solidified particles. It must be noted that the detection limit of the porosity is the same as the X-ray tomography beam resolution. In Al-Cu alloys, it has been shown that the porosity distribution of the Al-5wt%Cu and Al-17wt%Cu are very different. A 3D micro-porosity distribution within the droplet was generated using the Avizo™ software. Figure 21-16 shows this porosity distribution. Porosity distribution was found to be homogeneous in Al-5wt%Cu whereas in Al-17wt%Cu it is highly heterogeneous and polarized in the periphery. The porosity distribution within the droplets could be explained as follows. Lower alloy content sample has a higher growth rate of dendrites immediately after undercooling and nucleation of the primary α-Al phase. It also experiences a larger freezing range between liquidus and eutectic temperatures. Thus, the dendrites have more time to coarsen in a lower alloy content material. For the Al-Cu

Contairnerless Unidercooling of Drople and Droples. Edited by D.M. Herlach and D. M. Matson
Copyright © 2011 WILEY-VCH Verlag GmbH & Co. KGaA, Weinheim
ISBN 978-3-527-33122-2

system, the Al-5wt%Cu will also have less liquid to solidify as eutectic than the Al17%Cu sample. Thus, in Al-17wt%Cu sample, thinner dendrites and a larger fraction of liquid enable the liquid to be fed into interdendritic regions during solidification. This leaves the final shrinkage porosity to occur near the periphery of the droplet, coincident with the location of the final liquid in the droplet to solidify. This is apparent in Figures 21-14 where both eutectic and porosity are visualized and in Figure 21-16 contrasting the porosity in Al-5wt%Cu with that in Al-17wt%Cu.

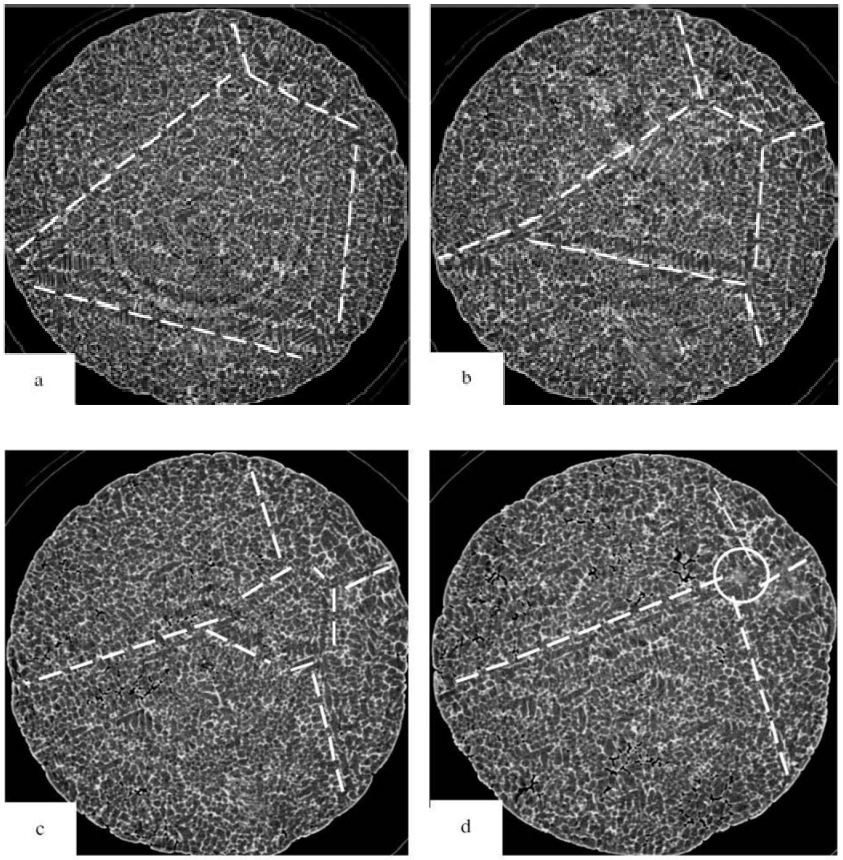

Figure 21-15: The progressive movement of a multiple equiaxed pattern (white dotted lines) converging to a nucleation site in Al5wt%Cu droplet. The encircled region in (d) shows the nucleation site. (a), (b), (c) and (d) are image numbers 430, 460, 495 and 520, respectively, out of a stack of 660 for a 660 µm Al5wt%Cu droplet view along the axial direction [22].

Ilbagi et al. [4] also used X-ray micro-tomography to investigate the effect of cooling rate on the formation of the porosity. The micro-tomography experiments were carried out the beam line Tomcat, X02DA at Swiss Light Source, Paul Scherrer Institut, Villigen, Switzerland. It was found that porosity tends to form closer to the periphery in droplets cooled in helium compared with those cooled in nitrogen, as is visualized using the software Avizo ™ in Figure 21-17. In this figure, two 328 µm diameter particles are shown. The particle in Figure 21-17a was atomized in helium while the particle in Figure 21-17b was atomized in nitrogen. The average volume fraction of porosity was also quantified. The procedure involves calculating the number of pixels with gray scale levels matching that of porosity within the entire droplet volume. Quantitative analysis of these images revealed that the volume percent of the porosity decreases if helium is used instead of nitrogen. The mechanism responsible for this difference in porosity distribution and amount is likely the same as was discussed above with Cu content in an Al alloy. That is the dendrite growth rates in the He atmosphere are

Contairnerless Unidercooling of Drople and Droples. Edited by D.M. Herlach and D. M. Matson
Copyright © 2011 WILEY-VCH Verlag GmbH & Co. KGaA, Weinheim
ISBN 978-3-527-33122-2

higher than in a N_2 atmosphere. This will result in a fine structure thus making it easier for liquid to feed regions that have already solidified and are liquid poor.

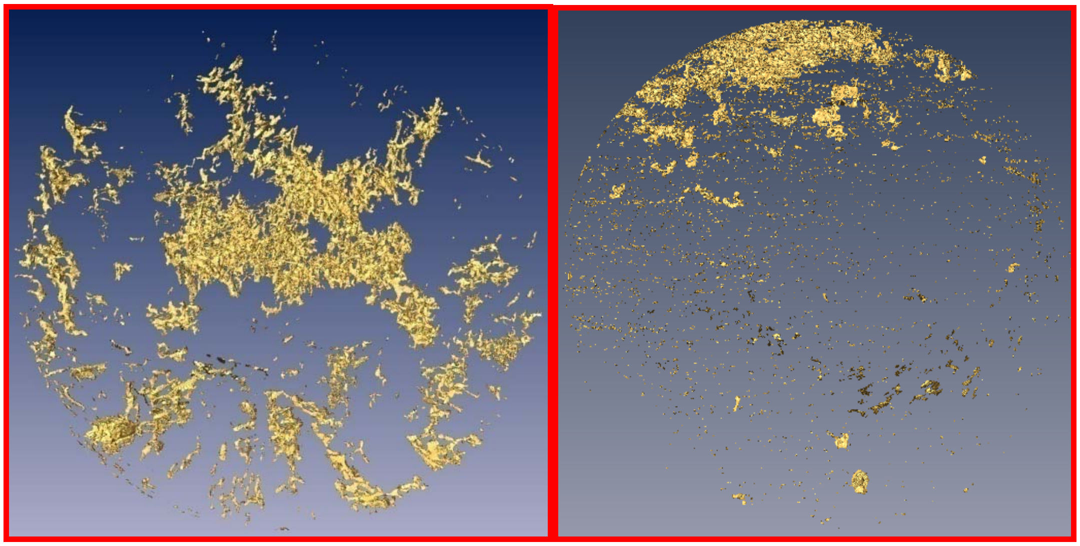
(a) (b)

Figure 21-16: 3D porosity distribution for (a) Al-5wt%Cu and (b) Al-17wt%Cu droplets. The homogeneous distribution in Al-5wt%Cu droplet is markedly different from the peripheral distribution in the Al-17wt%Cu droplet.

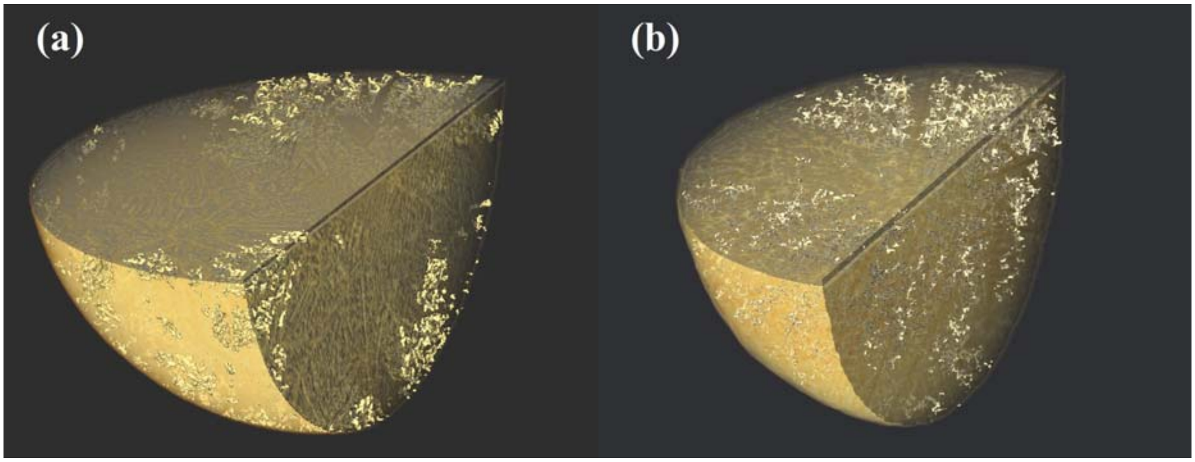

Figure 21-17. Visualization of the porosity within two particles of 328 μm diameter, atomized in helium (a) and nitrogen (b) [4].

21.4.3. Neutron Diffraction

Bulk penetration by neutrons provides information about the entire volume of the droplet, whereas X-ray diffraction is primarily a near-surface analysis. Due to the anisotropy visible in powder structure observed in 3D micro-tomography, clearly 3D bulk diffraction information is required in order obtain a representative analysis of rapdly solidified samples. For powders generated using IA, neutron diffraction has been used for phase identification and phase quantification using Rietveld analysis.

Prasad et al. [25] quantified microsegregation for the rapid solidification of Al-Cu alloys. IA was used to generate Al-Cu alloys of three nominal compositions, 5 wt% Cu, 10 wt% Cu and 17 wt% Cu under Nitrogen

Contairnerless Unidercooling of Drople and Droples. Edited by D.M. Herlach and D. M. Matson
Copyright © 2011 WILEY-VCH Verlag GmbH & Co. KGaA, Weinheim
ISBN 978-3-527-33122-2

and Helium gas. This quantification requires application of Rietveld analysis on neutron diffraction data that provides weight percent of $CuAl_2$, as well as stereology calculation on SEM images that yields volume percent of eutectic. Using these data, it is possible to determine the weight percent eutectic. Figure 21-18 shows the variation of weight percent of eutectic as a function of alloy composition. Note that this plot is different than Figure 21-10, where the volume fraction of eutectic from image analysis was plotted as a function of particle size. In Figure 21-18, each data point represents a droplet size atomized under a given gas type, and therefore represents the effect of cooling rate. Solid data points represent He gas whereas the hollow points represent N_2. Scheil-Gulliver and equilibrium predictions are also presented in Figure 21-18. Clearly, there is a distinct relative decrease in microsegregation with increasing composition as seen by the increasing difference between experimentally determined amount of eutectic or $CuAl_2$ and the Scheil-Gulliver prediction. Furthermore, there is only a small effect of cooling rate on the microsegregation and it is not as significant as the effect of alloy composition on microsegregation.

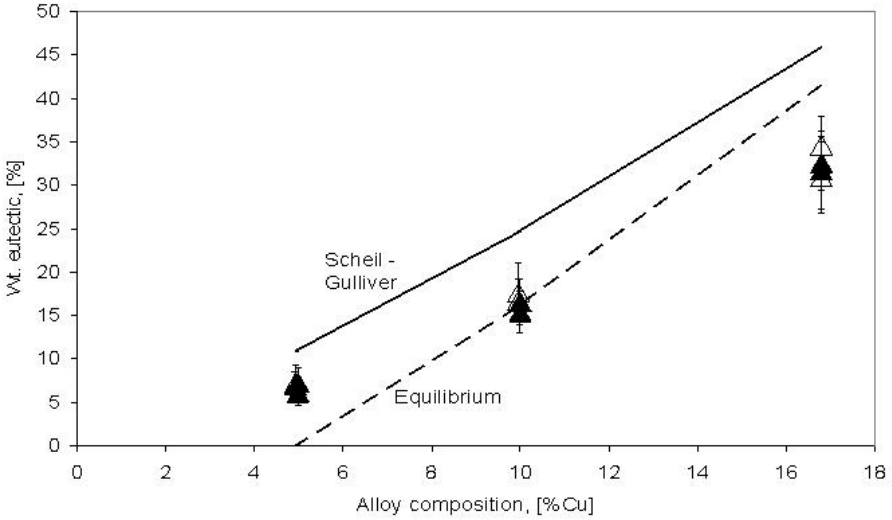

Figure 21.18: Weight percent eutectic in the atomized droplets as a function of alloy composition. Solid points are for the He atomized droplets while the open points represent droplets atomized under N_2 [25].

Using the weight percent eutectic and weight percent $CuAl_2$ in mass and volume balance equations one can also calculate the average solute solubility in the primary phase. Figure 21-19 shows the value of the average Cu solubility in the primary phase. The data are shown for two different droplet sizes and two gas types for all the alloy compositions. This shows the effect of gas type and droplet size more readily. It can be seen that there is a small effect of gas type on the amount of Cu disolved in the primary phase can hold, whereas the strong effect of alloy composition in solubility is clearly seen.

Contairnerless Unidercooling of Drople and Droples. Edited by D.M. Herlach and D. M. Matson
Copyright © 2011 WILEY-VCH Verlag GmbH & Co. KGaA, Weinheim
ISBN 978-3-527-33122-2

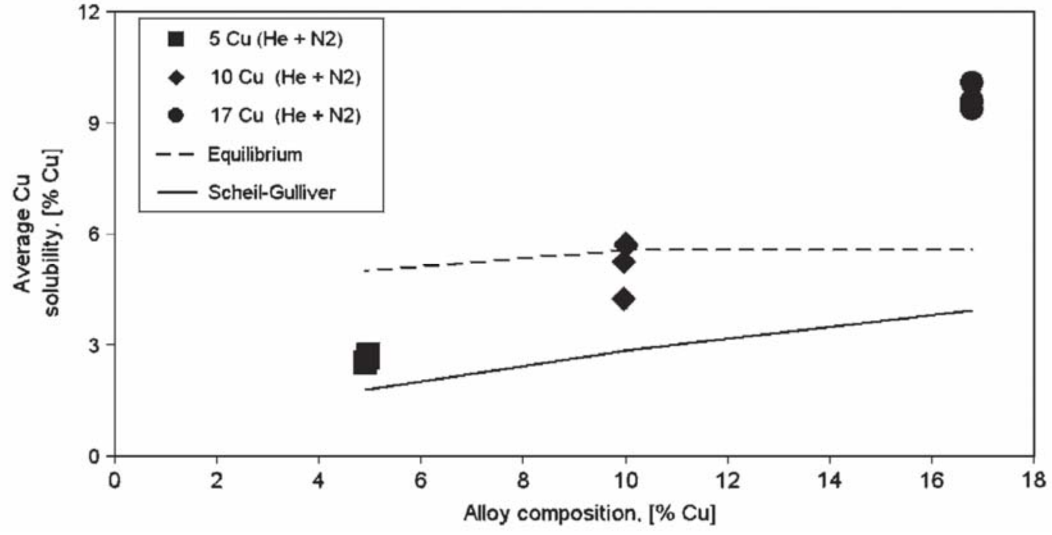

Figure 21.19. Cu solubility in the primary phase plotted for droplets of the three alloy compositions. The strong effect of alloy composition in solubility is clearly seen [25].

21.5. Modeling

21.5.1 Cooling rate

Interpretation of the solidification microstructure of IA droplets requires an understanding of the thermal transport between a droplet and its surrounding gas. Considering the complexity of melt atomization, heat transfer analysis has been generally confined to the study of a single droplet moving with respect to a gas.

In a single fluid atomization system, droplets form when exiting the orifice with a known initial velocity. Subsequent trajectory of the droplets depends on the values of the initial velocity, on gravity and on drag. The instantaneous acceleration of the droplet can be found by balancing the applied forces on a droplet as follows [26].

$$\frac{dv}{dt} = \frac{\rho_s - \rho_g}{\rho_s} g - 0.75 \frac{\rho_g}{\rho_s} \frac{C_d}{D_s} v^2 \qquad (1)$$

where v is the relative velocity between the droplet and the atomization gas, which in the case of IA $v_{gas}=0$, ρ_s and ρ_g are the densities of the droplet and atomizing gas, respectively. D_s is the droplet diameter, $C_d = \frac{18.5}{\mathrm{Re}^{0.6}}$ [18], $\mathrm{Re} = \frac{\rho_g v D_s}{\mu_g}$ and μ_g is the gas viscosity.

An equation describing the rate of heat energy lost at the droplet surface is given by Eq. 2

$$q = h_{eff} A (T_s - T_g) \qquad (2)$$

where h_{eff} is the effective heat transfer coefficient and consists of the additive contribution of convection, conduction and radiation heat transfer mechanisms, A is the surface area of the droplet, T_s is the droplet surface temperature and T_g is the free stream gas temperature. For low temperature alloys (e.g. aluminum based alloys) the effective heat transfer is dominated by convection, while for high temperature alloys (e.g. iron based alloys) radiation heat transfer can be significant.

The complexity of Eq. 2 is in determining the h_{eff}. The effective heat transfer coefficient is a complicated function of the thermophysical properties of the gas medium, the size of the droplet and its relative velocity

Contairnerless Unidercooling of Drople and Droples. Edited by D.M. Herlach and D. M. Matson
Copyright © 2011 WILEY-VCH Verlag GmbH & Co. KGaA, Weinheim
ISBN 978-3-527-33122-2

with the gas, particularly, the velocity and temperature profiles in the gas boundary layer surrounding the droplet. One approach to quantify the convective component (H_c) of h_{eff} has been through the use of semi-empirical equations (e.g. Ranz-Marshall or Whitaker) [27, 28] where Nusselt number (*Nu*) is averaged over the entire droplet surface. Eq. 3 shows a general form of such equations.

$$Nu = \frac{H_C D_s}{k_g} = A + B.\mathrm{Pr}^m.\mathrm{Re}^n \qquad (3)$$

Where $\mathrm{D_s}$ is the droplet diameter, $\mathrm{Pr} = \frac{Cp_g \mu_g}{k_g}$, k_g, Cp_g ρ_g and μ_g are the conductivity, heat capacity, density and viscosity of the gas, respectively, and all other parameters are constants. However, the coefficients A and B in Equation (3) were not derived for high temperature conditions such as atomized droplets, where there is a significant temperature gradient across the boundary layer in the surrounding gas. This temperature gradient can significantly vary the thermophysical properties of the gas. Wiskel et al. [29] quenched the falling droplets at various heights to find the range of heights at which various sizes of particles are fully solidified and compared it with the predicted height using Ranz-Marshall and Whitaker equations. They found that these equations significantly underestimate the heat transfer conditions when they evaluate the gas properties only at the ambient or film temperature alone, where film temperature is the average of surface and ambient temperature. Hence, they modify the Whitaker correlation in a way that it takes into account the variability of the gas conductivity across boundary layer. This variability in gas conductivity becomes important as the relative velocity between gas and atomized metal droplet and a cooling gas approaches zero (i.e. Re approaches zero). Using the modified Whitaker correlation (Eq. 4)

$$Nu = \frac{h_C D_s}{k_g} = 2\frac{C}{k_s(m+1)} \cdot \frac{\left(T_s^{m+1} - T_g^{m+1}\right)}{\left(T_s - T_g\right)} + \left(0.4\,\mathrm{Re}^{1/2} + 0.06\,\mathrm{Re}^{2/3}\right)\mathrm{Pr}^{0/4}\left(\frac{\mu_g}{\mu_s}\right) \qquad (4)$$

where C is the pre-power coefficient from the variation of gas conductivity with temperature and m is the power coefficient in the same equation (e.g. for nitrogen $C = 3.44\times10^{-4}$ and $m = 0.7609$ [29]), the model was able to closely predict the range within which the particles completely solidified under the condition that k_s be evaluated at the metal droplet surface temperature and the *Re* and *Pr* numbers at the free stream gas temperature.

The modified Whitaker correlation has since been used in modeling the solidification during metal droplet falling (e.g. [7, 30]). It must be noted that the modified Whitaker correlation does not take into account the chemical segregation within the alloy droplet.

In a different work, Prasad and Henein [31] combined the heat transport model (called thermal model hereafter) with a microsegregation model, described below, to pinpoint the effect of process variables on heat losses from the droplets. In that work, the effect of gas type, droplet size, gas temperature, gas-droplet relative velocity on the heat transport from the solidifying droplets was examined. In their model, the rate of heat extraction is assessed by calculating the cooling rate of a solidifying droplet. The model can be used with a zero or non-zero primary phase nucleation undercooling. For the case of zero undercooling, the cooling rate is defined as $(T_{liq}\text{-}T_{sol})/t_f$, where T_{liq} and T_{sol} are liquidus and solidus temperatures, respectively and t_f is the solidification time. Let us call this definition, "Definition I" of cooling rate. When the primary phase undercooling is non-zero "Definition II" of cooling rate is defined as $(T_{nuc}\text{-}T_{sol})/t_f$, where $T_{nuc}=T_{liq}\text{-}T_u$ and T_u is the degree of undercooling. The microsegregation model discussed in more detail in Chapter 19 uses the Rappaz-Thevoz microsegregation model [32] for a single equiaxed grain, growing like a spherical envelope in an undercooled droplet. Within this

Contairnerless Unidercooling of Drople and Droples. Edited by D.M. Herlach and D. M. Matson
Copyright © 2011 WILEY-VCH Verlag GmbH & Co. KGaA, Weinheim
ISBN 978-3-527-33122-2

spherical grain, the solute mass transport takes place between the dendritic solid and interdendritic liquid. LKT dendrite kinetics [33] is also utilized to account for the rate of growth of the solid-liquid interface. As the entire droplet is covered by the envelope, the remaining liquid solidifies according to Scheil-Gulliver model and subsequently, eutectic solidification completes the process. The initial values for this model are melt temperature, droplet initial velocity, material and gas property, nucleation undercooling of the primary phase as well as nucleation position. Two primary nucleation nucleation undercoolings of 0 and 20K were chosen, based on previous modeling work [26], and a nucleation position was placed in between the droplet center and periphery at exactly 0.5R, where R is the droplet radius [26].

The model was applied to two droplet sizes (350 μm and 50 μm) of Al-1.43wt%Si, atomized under two gases (He and N_2) at two different gas temperatures (T_{gas}=300K and 800K) with 0.5 m/s initial velocity. They calculated the cooling rate under the following scenarios,

1. Thermal model, 0 K primary nucleation undercooling (using Definitin I) and 20 K primary nucleation undercooling (using both Definition I and Definition II).

2. Microsegregation model, 20 K primary nucleation undercooling (using Definition II)

Their results showed that under the conditions investigated, the presence of undercooling does not significantly affect the cooling rate when it is calculated using the thermal model and under Definition I (i.e. See Table 21-1, column IV and V). Although a wide range of cooling rates were studied, only a difference in the order of 3-4% in the achieved cooling rates was observed. Also, their results showed that the use of thermal or microsegregation model, under Definition II also does not make a significant difference in cooling rate (i.e. column VI and VII). Therefore, they decided, for further analysis, to use the cooling rate results from the thermal model with 0 K undercooling with Definition I and microsegregation model with 20 K undercooling with Definition II of cooling rate, as highlighted on Table 21-1.

Table 21-1. Cooling rate results from thermal and microsegregation models [31].

Gas	T_{gas} (K)	Droplet size (μm)	Cooling rate (K/s)			
			Thermal Model			Microsegregation Model
			0K, Def. I	20K, Def.I	20K, Def II	20K, Def II
N_2	800	350	59	61	44	42
		50	1,834	1,886	1,350	1,299
	300	350	368	384	274	277
		50	9,504	9,844	7,055	6,726
He	800	350	226	233	166	165
		50	9,448	9,766	6,957	6,877
	300	350	1,142	1,188	847	871
		50	45,195	49,397	33,293	33,478

Table 21-2 shows the ratio of calculated cooling rates between thermal and microsegregation model (the highlight columns of Table 21-1). The results are shown for two different initial velocities of 0.5 m/s and 30 m/s under He and N_2 gases at 300 K and 800 K, respectively. It is evident that the thermal model consistently gives higher cooling rates for all cases. This is true for both gas types, gas temperatures and for either initial droplet velocities.

Contairnerless Unidercooling of Drople and Droples. Edited by D.M. Herlach and D. M. Matson
Copyright © 2011 WILEY-VCH Verlag GmbH & Co. KGaA, Weinheim
ISBN 978-3-527-33122-2

Table 21-2 Ratio of cooling rates for different conditions obtained from the thermal and microsegregation model [31]

Gas temp. (K)	Ratio of cooling rate between thermal and microsegregation model			
	0.5 m/s		30 m/s	
	He	N_2	He	N_2
300	1.31	1.33	1.31	1.33
800	1.37	1.41	1.38	1.45

The solidification time, t_f, was also calculated for a 350 μm droplet cooled under He gas at 300 K and 800 K for two different initial droplet velocities. It can be seen that the microsegregation model gives solidification times that are marginally smaller than those from the thermal model. It has to be noted that the calculated generated heat from the two models are different as the dendrite kinetics governs the latent heat release for part in the microsegregation model.

Table 21-3. The solidification times from thermal and microsegregation models for a 350 μm droplet cooled under He gas at two different gas temperatures and two different initial velocities [31].

Gas temp. (K)	0.5 m/s		30 m/s	
	Thermal (s)	Microsegregation (s)	Thermal (s)	Microsegregation (s)
300	0.060	0.057	0.025	0.024
800	0.308	0.301	0.222	0.219

The microsegregation model also showed that the dendrite velocity for a 350 μm droplet in He at 300 K can reach up to 1.8 cm/s at the onset of recalescence. It then reduces down to 0.6 cm/s as the latent heat is released. This reduction in dendrite velocity as well as occurrence of the isothermal eutectic tend to lengthen the total solidification time in the way that it is seen in Table 21-3, where the results from the thermal model and the microsegregation model are very close. Also, the cooling rate from microsegregation model is lower because the presence of 20 K of primary undercooling reduces the freezing range. Hence according to the Definition II of cooling rate, the cooling rate from microsegregation is consistently lower even when the solidification time is almost the same from the two models. The freezing range of the alloy studied is approximately 70 K and when one considers a 20 K undercooling, the freezing range reduces by almost 30% for Definition II (microsegregation model) as compared to Definition I (thermal model). This can explain the 1.3–1.4 ratio between the thermal and the microsegregation models. In summary, the presence of undercooling or the use of thermal or microsegregation model does not affect the cooling rate analysis. Also, from Tables 21-1 to 21-3, it is evident that the droplet diameter and gas temperature are the two most important variables in transport between droplet and gas. Prasad and Henein also showed that for the larger particles (<200 μm) the temperature driving force between gas and droplet temperature is the most critical variable. For droplets <200 μm the droplet diameter becomes a significant variable [31].

21.5.2 Eutectic Undercooling

As was shown in Figure 21-10 the experimental results for the volume percent of $CuAl_2$ in alloys of Al with 5 and 10 wt.% Cu are above the equilibrium line while those at 17 and 24 wt.% Cu are below. Prasad et al. [34] used the microsegrgation solidification model to investigate these results. Tables 21-4 and 21-5 show the properties of the alloys and the initial values used in the simulations. The value of dendrite undercooling listed in Table 21-5 is obtained from a quantification of 3D micro-tomography images such as those shown in Figure 21-15. The region circled in Figure 21.5d identifies the area of initial growth that occurs after nucleation but before the onset of recalescence. The volume of this region is quantified from 3D micro-tomography images. The microsegregation mdel is then excecuted for a range of undercoolings for primary α-Al. It was found that a 15°C undercooling in the model yielded a volume of initial growth in agreement with the measured value.[34] The eutectic undercoolings were estimated for the solute content shown in Table 21-5 using experimental measurements on Al-Cu droplets processed in the terrestrial Electomagnetic Levitator.[35]

Table 21-4. Properties of alloys used in the simulation [34].

Alloy properties	4.3%Cu	5%Cu	10%Cu	17%Cu
Liquidus temperature [K]	922	920	907	885
Density [kg m^{-3}]	2750	2760	2870	3100
Specific heat [J K^{-1} m^{-3}]	$3.2378 \cdot 10^6$	$3.2465 \cdot 10^6$	$3.3087 \cdot 10^6$	$3.3957 \cdot 10^6$
Latent heat [J m^{-3}]	$10.8113 \cdot 10^8$	$10.8661 \cdot 10^8$	$11.2575 \cdot 10^8$	$11.8054 \cdot 10^8$
Liquidus slope [K $(\%)^{-1}$]	-3.63	-3.66	-3.86	-4.23
Partition coefficient [-]	0.177	0.178	0.194	0.224

Table 21-5. Initial values used in the simulations [34].

Parameters		Value
Melt temperature [K]		1123
Initial droplet velocity [ms^{-1}] [17]		0.5
Gas temperature [K]		303
Dendritic nucleation undercooling, ΔT_N^p [K]		15
Eutectic nucleation undercooling, ΔT_N^e [K]	5wt%Cu	20
	10wt%Cu	20
	17wt%Cu	27.5

From the experimental results (also shown in Figure 21-18), equilibrium phase diagram, Scheil-Gulliver model and microsegregation model they estimated the weight percent of the eutectic within the microstructure of solidified IA droplet. The results are shown in Figure 21-20. In the model, initially it is assumed that the eutectic transformation occurs at the equilibrium temperature given by the phase diagram. As can be seen, the predictions of the model (X's) are almost superimposed with the Scheil-Gulliver approximation, confirming the minor role played by solid state diffusion and the undercooling and nucleation of the primary α-Al phase.

Copyright © 2011 WILEY-VCH Verlag GmbH & Co. KGaA, Weinheim
ISBN 978-3-527-33122-2

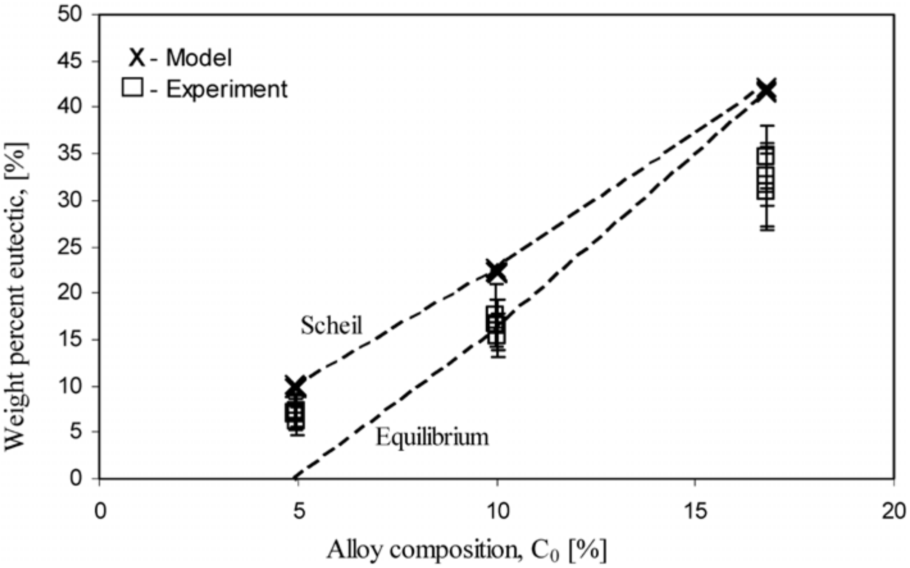

Figure 21-20: Comparison of the weight percent eutectic from experiments and model. In the model it was assumed that eutectic occurs at equilibrium under iso-thermal condition [34].

Both the Scheil-Gulliver approximation and the microsegregation model overestimate the weight percent of the eutectic. Eutectic undercooling was found to play an important role in microsegregation. The nucleation undercooling for the eutectic microstructure given in Table 21-5 was used to account for the eutectic undercooling. It was assumed that the dendritic structure can continue to form below the eutectic temperature and as a result, less liquid is available to grow the eutectic structure at a lower temperature. Good agreement is reached with experimental measurements (See Figure 21-21).

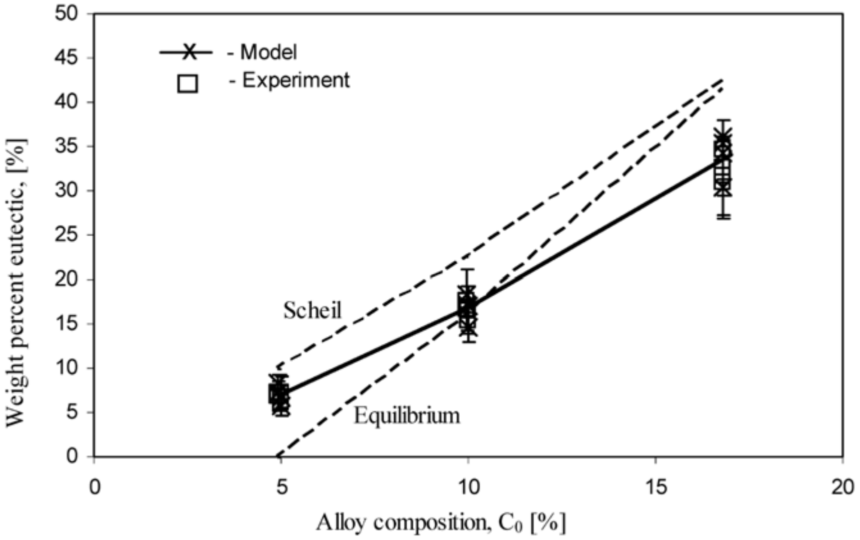

Figure 21-21. Comparison of weight percent eutectic between model and experiment. The model was run with estimated eutectic undercooling shown in Table 21-5[34].

Eutectic undercooling has also been reported in Al-Fe droplets of 0.6 wt%Fe and 1.9wt% Fe [19]. The former composition is hypoeutectic and the latter is hypereutectic. The microstructure of both samples was very similar predominantly composed of the primary α-Al phase with interdendritic eutectic. The intermetallic in the eutectic was believed to be Al_mFe where m is about 4. Using a modified phase diagram based on this

Contairnerless Unidercooling of Drople and Droples. Edited by D.M. Herlach and D. M. Matson
Copyright © 2011 WILEY-VCH Verlag GmbH & Co. KGaA, Weinheim
ISBN 978-3-527-33122-2

intermetallic composition and using an extension of the solidus and liquidus curves from the phase diagram, the eutectic undercooling was determined to be 10 and 17 °C for the Al-0.6 wt% Fe and for the Al-1.9wt%Fe alloys, respectively. More detailed microstructural characterization of these Al-Fe IA powders was reported using TEM, Neutron diffraction and EBSD [36]. The TEM analysis confirmed that the metastable Al_mFe intermetallic was present in the powders of both compositions. Based on the neutron diffraction results, it was reported that the powders had considerable texture. This implies that the primary phase α-Al is strongly oriented. This can arise due to the fast growth of the primary phase after nucleation and during recalescense. However, Gandin et al had predicted [37] that with IA Al-Cu powders, a portion of the structure formed during recalescence would re-melt, leading to grain multiplication following the end of recalescence. The fraction of solid that would remelt was reported to be a function of the amount of primary phase undercooling. EBSD analysis was carried out by Chen et al [36] on the Al-0.6 wt% Fe and the Al-1.9wt%Fe IA powders. A sample result of the EBSD characterization is shown in Figures 21-22.

Figure 21-22-A is an optical image of one of the IA Al-0.6wt% Fe particles. In this image three primary trunks are visible and intersect to the right of the centre of the particle. The remainder of the particle are secondary dendrite. A close up view of the region near the point of intersection of the three primary trunks is shown in 21-22-B. The point of intersection of the trunks is used as the reference point for misorientation. The color in the rest of the image in 21-22-C is related to the relative misorientation of the structure with respect to the point of reference. The scale of this relative misorientation is shown at the bottom of (C). Clearly most of the structure has the same orientation as the point of reference. This confirms the high degree of texture measured from the Neutron Diffraction results. However, there are a small number of regions that have up to 10 degrees of misorientation to the reference point. These indicate that these dendrites experienced remelting likely during recalescence. This confirms the predictions of remelting proposed by Heringer et al [37]. Figure 21-22-D shows the pole figures for the same region in (C). The colours also represent the same relative misorientations presented in (C). The pole figures show a strong cubic texture. Similar results were reported [36] for the Al-1.9wt%Fe sample but there was a noticeably lower fraction of solid that was misoriented. The Al-1.9wt% Fe sample demonstrated stronger texture that the Al-0.6 wt% Fe sample.

The contoured version of the <111> pole figures for Al-0.6 wt% Fe and Al-1.9wt% Fe samples is shown in Figure 21-23 (A) and (B) respectively. Four of the five poles in the Al-0.6wt%Fe sample are at a radial distance of 68°, 82°, 112°, and 82°. The pole close to the center indicats that the growth direction was <111>. For the Al-1.9wt%Fe sample (B) the pole closer to the centre than in Al-0.6 wt%Fe sample. This dendritic growth direction cannot at present be explained. More systematic studies of the relationship between growth direction and undercooling is needed.

21.5.3 Peritectic Systems

IA technique has been used to study solidification in peritectic systems such as Al-Ni [24, 38]. Al-36 wt%Ni and Al-50 wt%Ni was impulse atomized in helium and nitrogen. The resulting powders were sieved into different size ranges. The secondary dendrite arm spacing (SDAS) measurement was done on the various particle sizes. Figure 21-22 shows the results of the changes of SDAS against particle size. It is evident that the decrease of particle size and use of helium rather than nitrogen result in refinement of the microstructure.

Neutron diffraction was used in order to quantify the phase fractions in the samples. Profile refinement using the computer software GSAS (General Structure Analysis System) was used to calculate the weight fraction of the existing phases, namely Al_3Ni_2, Al_3Ni and Al. Figure 21-24 shows the weight fraction ratio of Al_3Ni to Al_3Ni_2 as a function of increasing particle size.

Contairnerless Unidercooling of Drople and Droples. Edited by D.M. Herlach and D. M. Matson
Copyright © 2011 WILEY-VCH Verlag GmbH & Co. KGaA, Weinheim
ISBN 978-3-527-33122-2

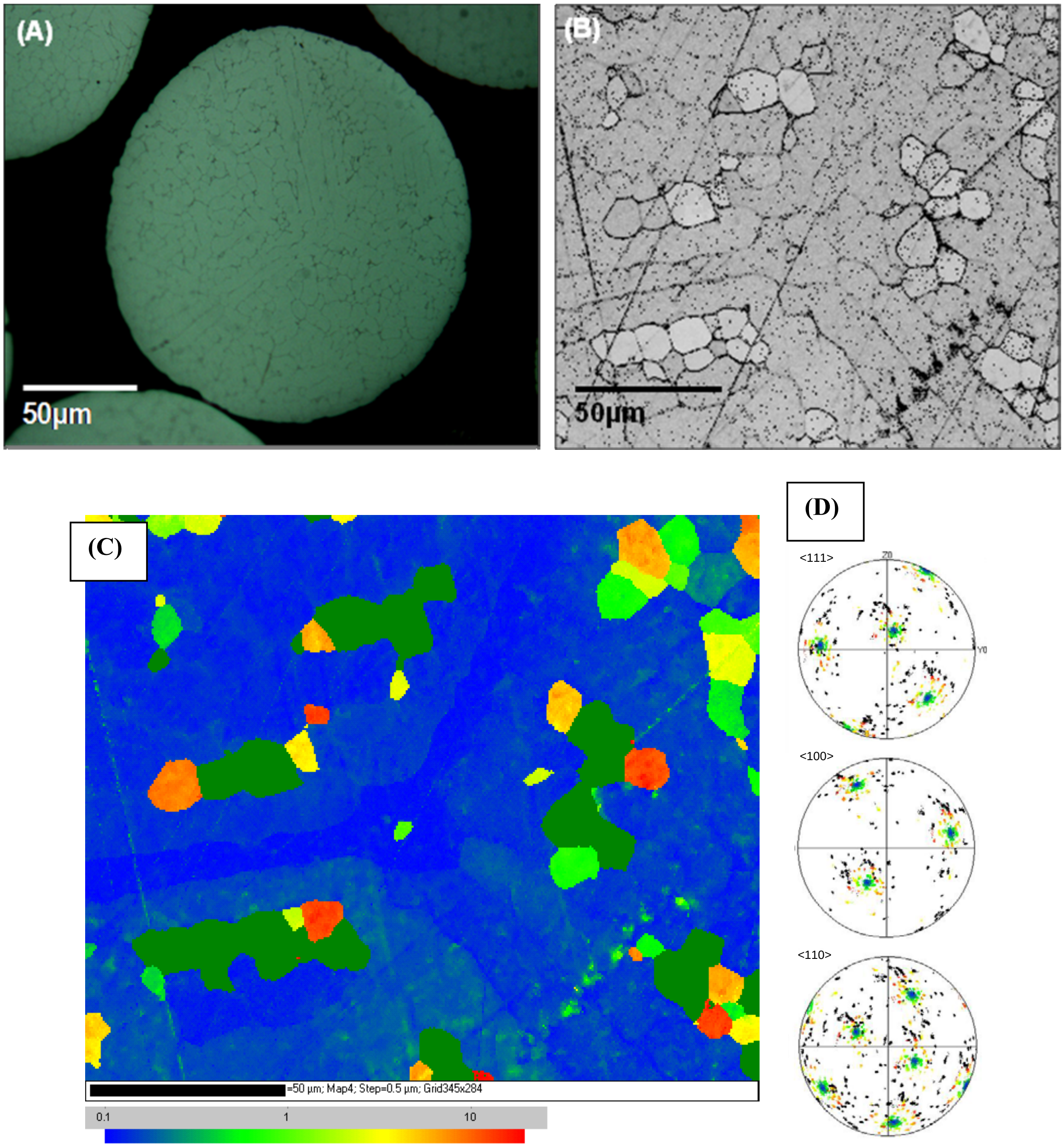

Figure 21-22: (A) is an optical image of an IA Al-0.6 wt% Fe selected for EBSD characterization. (B) displays the band contrast EBSD image for a region that appears to contain a nucleation site and the primary and side dendrites. (C) is the EBSD reconstructed image for the region shown in Figure 6 (B). The legend at the bottom of (C) indicates degree of misorientation in the structure. (D) illustrates <111>, <100> and <110> pole figures obtained from the same region. Colors in the pole figures correspond to the region with the same color in (C). In the pole figures, Y_0 and Z_0 are coincident with the primary sample axes.[36]

Contairnerless Unidercooling of Drople and Droples. Edited by D.M. Herlach and D. M. Matson
Copyright © 2011 WILEY-VCH Verlag GmbH & Co. KGaA, Weinheim
ISBN 978-3-527-33122-2

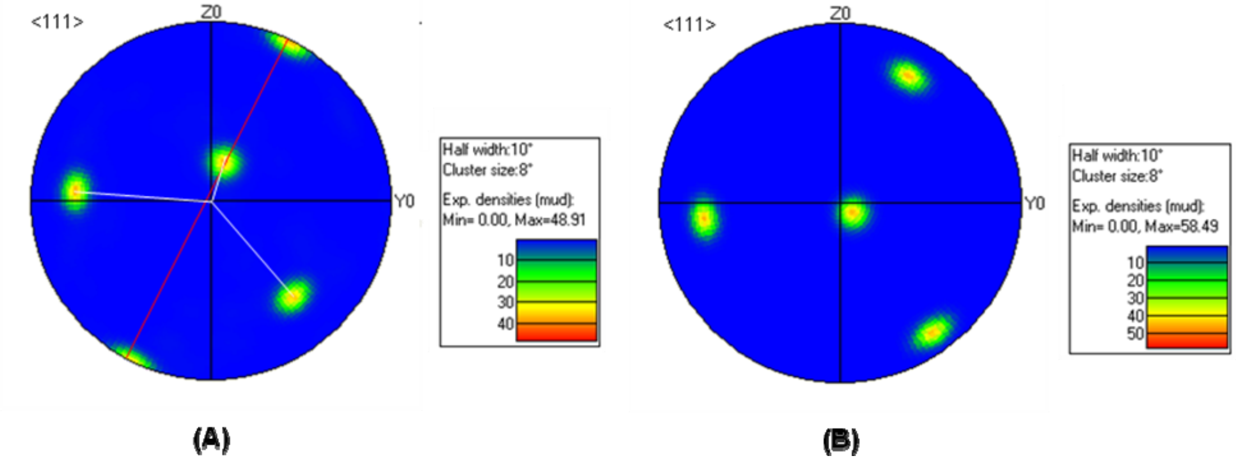

Figure 21-23: Representation of <111> pole figures (contoured version) of Al-0.61wt% Fe (A) and Al-1.9 wt% Fe (B).[36]

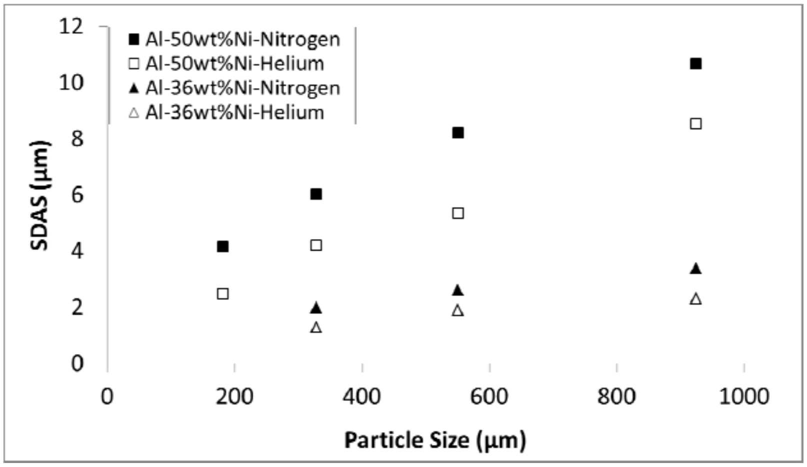

Figure 21-24: Effect of particle size, gas type and composition on SDAS [38].

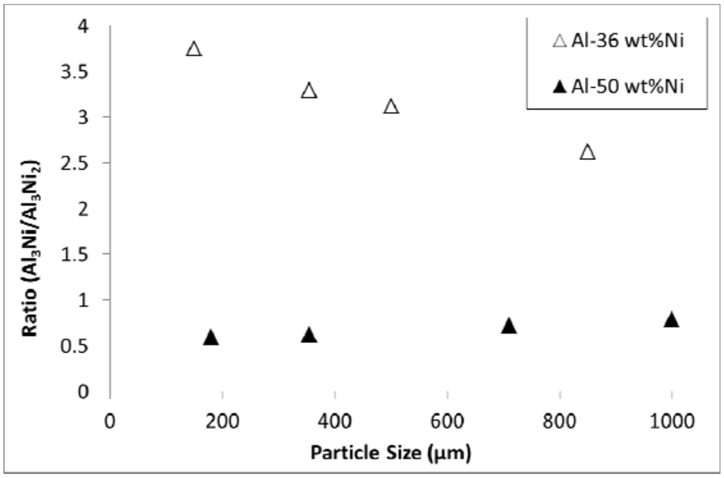

Figure 21-25: Neutron diffraction results for ratio of Al_3Ni to Al_3Ni_2 as function of particle size for for two Al-Ni alloys cooled in helium.

It can be seen that by increasing the particle size in Al-50 wt%Ni the ratio of Al_3Ni/Al_3Ni_2 slightly increases. This can be due to the slow rate of peritectic transformation Al_3Ni_2+liquid→Al_3Ni [39]. Therefore with increasing particle size, and hence, decreasing cooling rate, more time is available for this time dependent transformation.

In the particles of Al–36 wt%Ni, with increasing particle size, the ratio Al_3Ni/Al_3Ni_2 decreases. It is likely that increasing cooling rate as a result of decreasing particle size results in the suppression of the primary Al_3Ni_2. Further investigation of the microstructure of small particles of Al-36 wt%Ni can prove this hypothesis. Figure 21-27 shows a microstructure of a 328 µm diameter particle and Figure 21-26 shows the microstructure of a 150 µm particle both cooled in helium. While the microstructure shown in Figure 21-26 clearly shows the formation of the peritectic phase around the primary phase, in Figure 21-27 a completely different microstructure, which is a characteristic of Al_3Ni that directly forms from liquid is observed. The formation of the pro-peritectic phase Al_3Ni_2 was suppressed due to fast cooling rate in small particles of IA Al-36 wt%Ni. It remains to extend the microsegregation model developed for eutectic transformation to peritectic systems. While this peritectic microsegregation model has been validated for the solidification of an EML droplet, IA droplets present a more challenging validation due to their small size. A large volume fraction of a droplet undergoes rapid solidification than is the case with a 6 mm droplet processed in EML. By contrast, in the EML apparatus it is feasible to measure droplet undercooling and primary solid growth rates. Thus, both EML and IA-drop tube serve complimentary roles in studying and quantifying rapid solidification in alloys.

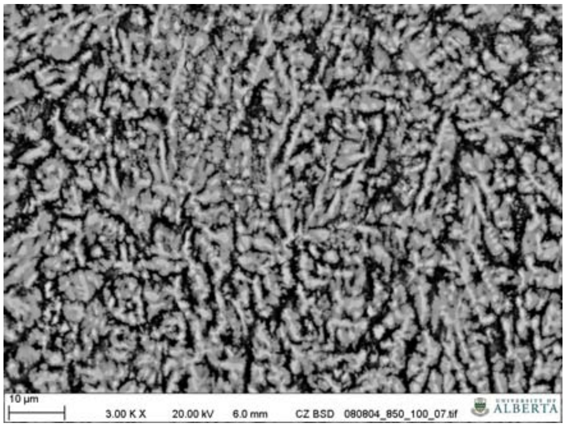

Figure 21-26: Al–36 wt-%Ni particle with diameter of 328 µm cooled in helium.[38]

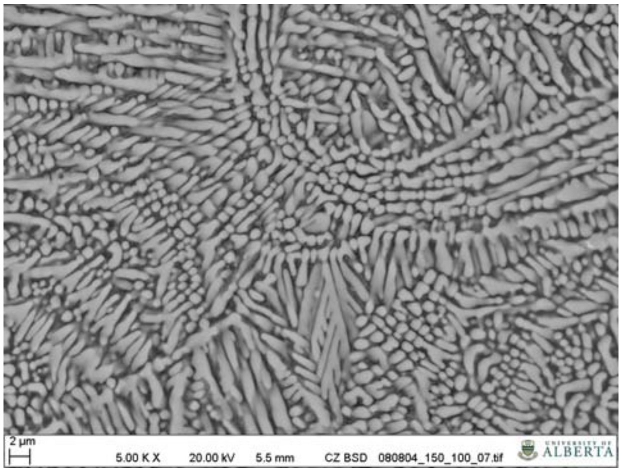

Figure 21-27: Al–36 wt%Ni particle with diameter of 150 µm cooled in helium [38].

Contairnerless Unidercooling of Drople and Droples. Edited by D.M. Herlach and D. M. Matson
Copyright © 2011 WILEY-VCH Verlag GmbH & Co. KGaA, Weinheim
ISBN 978-3-527-33122-2

References:

[1] T. Volkmann, W. Loser, D.M. Herlach, *Nucleation and phase selection in undercooled Fe-Cr-Ni melts. II. Containerless solidification experiments*, Metallurgical and Materials Transactions A **28**(2) (1997) 461.
[2] B. Vinet, L. Cortella, J.J. Favier, P. Desre, *Highly undercooled W and Re drops in an ultrahigh-vacuum drop tube*, Applied Physics Letters **58**(1) (1991) 97.
[3] T. van Zoest, N. Gaaloul, Y. Singh, H. Ahlers, W. Herr, S. T. Seidel, W. Ertmer, E. asel, M. Eckart, E. Kajari, S. Arnold, G. Nandi, W. P. Schleich, R. Walser, A. Vogel, K. engstock, K. Bongs, W. Lewoczko-Adamczyk, M. Schiemangk, T. Schuldt, A. Peters, T. Önemann, H. Müntinga, C. Lämmerzahl, H. Dittus, T. Steinmetz, T. W. Hänsch, and J. eichel, *Bose-Einstein Condensation in Microgravity*, Science **328** (5985) (2010) 1540.
[4] L. Chen, X.H. Luo, *A new way to explore microgravity effect by drop tube experiment*, Acta Metallurgica Sinica **43**(7) (2007) 769.
[5] J. Ziesenis, J. Tillwick, M. Krauss, V. Uhlenwinkel, *Atomization: fundamentals and practice*, eds. K.P. Cooper et al. (2000, TMS, Warrendale, PA), p. 61.
[6] J. Ting , J. Connor, S. Ridder, *High-speed cinematography of gas metal atomization*, Materials Science and Engineering A-Structural Materials Properties Microstructure and Processing **390** (2005) 452.
[7] A.V. Freyberg, H. Henein, V. Uhlenwinkel and M. Buchholz, *Droplet solidification and gas-droplet thermal coupling in the atomization of a Cu-6Sn alloy,* Metallurgical and Materials Transactions B **34** (2003) 243.
[8] A. Kawasaki, R. Watanabe and Y. Kuroki*, Preparation of monosized spherical powders of Pb-Sn alloy by pulsated orifice injection method*, Powder Metallurgy World Congress, Editions de Physique, Fr., (1994) P. 365.
[9] A. Miura, W. Dong1, M. Fukue, N. Yodoshi, K. Takagi2, A. Kawasaki, *Preparation of Fe-based monodisperse spherical particles with fully glassy phase,* Journal of Alloys and Compounds, **509** (2011) 5581.
[10] Q. Liu and M. Orme, *On precision droplet-based net form manufacturing technology*, Proceedings of the Institution of Mechanical Engineers, Part B: Journal of Engineering Manufacture **215** (2001) 1333.
[11] E.P. Muntz and M. Orme, *Charateristics, control and uses of liquid streams in space,* AIAA Journal **25** (1987) 746.
[12] P. Yim, J-H Chun, T. Ando and V.K. Sikka, *Production and characterization of mono-sized Sn-Pb alloy balls*, The International Journal of Powder Metallurgy **32** (1996) 155.
[13] D.Yuan*, The novel Impulse Atomization Process*, PhD thesis, University of Alberta (1997).
[14] L.C. Morin *et al.*, Impulse Atomization: *A Novel Technique to Economically Produce Powders with a Desired Size Distribution*, Adv. in PM & Particulate Mtls, APMI, Princeton, NJ, (1996) 1-185.
[15] K. Olsen *et al.*, *Upgrading Scrap Automotive Aluminum Alloys with the Impulse Atomization and Quench Technique*, Third International Symposium: Recycling of Metals and Engineered Materials, P.B. Queneau and R.D. Peterson, Eds, TMS, Warrendale, PA, (1995) 67.
[16] H. Henein, *Single fluid atomization through the application of impulses to a* melt, Materials Science and Engineering A **326** (2002) 92.
[17] Y. Ding, H. Henein and J. A. Fallavollita, *Methods and apparatus for producing droplets*, US Patent 5,609,919 (1997); Canadian Patent 2,147,407 (2003).
[18] J.B. Wiskel, K. Navel, H. Henein and E. Maire, *Solidification study of aluminum alloys using Impulse Atomization: Part II. Effect of cooling rate on microstructure*, Canadian Metallurgical Quarterly **41** (2) (2002) 193.
[19] H. Henein, V. Buchoud, R.-R. Schmidt, C. Watt, D. Malakhov, Ch.-A. Gandin, G. Lesoult, V. Uhlenwinkel, *Droplet solidification of impulse atomized Al-0.61Fe and Al-1.9Fe*, Canadian Metallurgical Quarterly **49**(3) (2010) 275.
[20] D. Yuan, J. Fallavollita, H. Henein and R. Eadie, *On the Generation of Narrow Sized Droplets by the Impulse Atomization Process*, Recent Developments in Non-Ferrous Pyrometallurgy, I.A. Cameron and J.M. Toguri, eds., Metallurgical Society of CIM (1994) paper 49.4.

Contairnerless Unidercooling of Drople and Droples. Edited by D.M. Herlach and D. M. Matson
Copyright © 2011 WILEY-VCH Verlag GmbH & Co. KGaA, Weinheim
ISBN 978-3-527-33122-2

[21] K. Conlon, E. Maire, D.S. Wilkinson and H. Henein, *Processing and microstructural characterization of Al-Cu alloys produced from rapidly solidified powders*, Metallurgical and Materials Transactions A **31** (2000) 249.
[22] A. Prasad, H. Henein, E. Maire, and C.A. Gandin, *X-ray tomography study of atomized al-cu droplets*, Canadian Metallurgical Quarterly, **43**(2) (2004) 273.
[23] A. Prasad, H. Henein, E. Maire, and C.A. Gandin, *Understanding the rapid solidification of al-4.3Cu and al-17Cu using X-ray tomography*, Metallurgical and Materials Transactions A, **37**(1) (2006) 249.
[24] A. Ilbagi, H. Henein and A. B. Phillion, *Phase quantification of impulse atomized Al68.5Ni31.5 alloy,* Accepted in J. Mater. Sci., (2010) DOI: 10.1007/s10853-010-4972-8.
[25] A. Prasad, H. Henein, and K. Conlon, *Quantification of microsegregation during rapid solidification of al-cu powders*, Metallurgical and Materials Transactions A, **37**(5) (2006) 1589.
[26] A. Prasad, *Microsegregation in rapidly solidified impulse atomized binary Al-Cu alloy*, PhD thesis, University of Alberta, (2006).
[27] W.E. Ranz and W.R. Marshall Jr, *Evaporation from drops*, Chem. Eng. Progress, **48**(3) (1952) 141.
[28] S. Whitaker, *Forced convection heat transfer correlations for flow in pipes, past flat plates, single cylinders, single spheres, and for flow in packed beds and tube bundles*, AIChE, **18**(2) (1972) 361.
[29] J.B.Wiskel, H. Henein, E. Maire, *Solidification study of aluminum alloys using impulse atomization: Part I - heat transfer analysis of an atomized droplet*, Canadian Metallurgical Quarterly, **41**(1) (2002) 97.
[30] R. Heringer, Ch.-A. Gandin, G. Lesoult, H. Henein, *Atomized droplet solidification as an equiaxed growth model*, Acta Materialia **54** (2006) 4427.
[31] A. Prasad and H. Henein, *Droplet cooling in atomization sprays*, J. Mater. Sci., **43** (2008) 5930.
[32] M. Rappaz, P.H. Thevoz, *Solute diffusion model for equiaxed dendritic growth*, Acta Metall. **35**(7) (1987) 1487.
[33] J. Lipton, W. Kurz, R. Trivedi, *Rapid dendrite growth in undercooled alloys*, Acta Metall. **35**(4) (1987) 957.
[34] A. Prasad, S. Mosbah, H. Henein and Ch.-A. Gandin, *A solidification model for atomization*, ISIJ International, **49**(7) (2009) 992.
[35] Ch-A Gandin, S. Mosbah, Th. Volkmann and D.M. Herlach, *Experimental and numerical modeling of equiaxed solidification in metallic alloys*, Acta Mater., **56** (2008) 3023.
[36] J. Chen, U. Dahlborg, C.M. Bao, M.-Calvo-Dahlborg and H. Henein, *Microstructure evolution of atomized Al-0.61 wt%Fe and Al-1.9 wt%Fe alloys,* Metallurgical and Materials Transactions B **42B** (2011) 557.
[37] R. Heringer, Ch.-A. Gandin, G. Lesoult and H. Henein, *Atomized droplet solidification as an equiaxed growth model,* Acta Materialia **54** (2006) 4427.
[38] A. Ilbagi, P. Delshad Khatibi, I. P. Swainson, G. Reinhart and H. Henein, *Microstructural analysis of rapidly solidified aluminium–nickel alloys*, in press Canadian Metallurgical Quarterly, **50**(3) (2011).
[39] D.H. St John, L.M. Hogan, *A Simple Prediction of the Rate of the Peritectic Transformation*, Acta Metallurgica, **35**(1) (1987) 171.

Contairnerless Unidercooling of Drople and Droples. Edited by D.M. Herlach and D. M. Matson
Copyright © 2011 WILEY-VCH Verlag GmbH & Co. KGaA, Weinheim
ISBN 978-3-527-33122-2